Atmospheric Research 285 (2023) 106636

Contents lists available at ScienceDirect

Atmospheric Research

journal homepage: www.elsevier.com/locate/atmosres

Sensitivity of the simulation of extreme precipitation events in China to different cumulus parameterization schemes and the underlying mechanisms

Shiyu Zhang [a,b], Minghao Wang [c,*], Lanning Wang [c], Xin-Zhong Liang [d], Chao Sun [d], Qingquan Li [b,e,**]

[a] Chinese Academy of Meteorological Sciences, Beijing 100081, China
[b] China Meteorological Administration Key Laboratory for Climate Prediction Studies, National Climate Center, Beijing 100081, China
[c] College of Global Change and Earth System Science, Beijing Normal University, Beijing 100875, China
[d] Department of Atmospheric and Oceanic Science, University of Maryland, College Park, MD 20740, USA
[e] Collaborative Innovation Center on Forecast and Evaluation of Meteorological Disasters, Nanjing University of Information Science and Technology, Nanjing, 210044, China

ARTICLE INFO

Keywords:
Extreme precipitation
Cumulus parameterization scheme
CWRF model

ABSTRACT

The ability of climate models to capture extreme precipitation events is crucially important, but most of the existing models contain significant biases for the simulation of extreme precipitation. To understand the causes of these biases, we used five different cumulus parameterization schemes in the regional Climate–Weather Research and Forecasting (CWRF) model to investigate its performance and biases in the simulation of extreme precipitation events in China. In general, the ensemble cumulus parameterization (ECP) scheme was the most skillful in reproducing the spatial distribution of the 95th percentile daily precipitation (P95) and the other four schemes either overestimated (the Kain-Fritsch Eta and Tiedtke schemes) or underestimated (the Betts-Miller-Janjic and New Simplified Arakawa-Schubert schemes) P95. Compared with the observational data, ECP scheme significantly improved the simulation of extreme precipitation in China and had the highest correlation and the smallest root-mean-square error in most areas and seasons. To clarify the underlying physical processes of P95 simulation biases, we established a regression model of extreme precipitation based on ECP scheme. This showed that P95 in North China is mainly affected by moisture convergence, planetary boundary layer height and lifting condensation level (relative importance 18–32%). In Central China, the vertical upward motion of water vapor, sensible heat flux and planetary boundary layer height (relative importance 18–30%) are main factors associated with P95. In South China, the vertical upward motion and horizontal transport of water vapor are predominant (relative importance 26–37%). In addition, the net surface energy, surface and atmospheric radiation flux, total precipitable water, convective available potential energy and cloud water path also have a high correlation with P95 (the second most important factor; relative importance 14–31%). The influence of each factor on the simulation of P95 is different when using different cumulus parameterization schemes and the interaction among the different factors determines the ability of CWRF model to simulate extreme precipitation. These results provide important references for future model evaluations and improvements.

1. Introduction

The Sixth Assessment Report of the Intergovernmental Panel on Climate Change (IPCC AR6) stated that extreme precipitation events have increased in most regions with the observational data since 1950. The annual variability of precipitation has also increased, mainly because the overall rate of increase in extreme precipitation events is faster than the average increase in precipitation, which brings challenges to the management of regional water resources (IPCC, 2021). According to the Clausius–Clapeyron equation, for each 1 °C of

* Corresponding author: College of Global Change and Earth System Science, Beijing Normal University, Beijing 100875, China
** Corresponding author at: National Climate Center, China Meteorological Administration, Beijing 100081, China.
E-mail addresses: wangmh0819@163.com (M. Wang), liqq@cma.gov.cn (Q. Li).

https://doi.org/10.1016/j.atmosres.2023.106636
Received 4 September 2022; Received in revised form 23 January 2023; Accepted 27 January 2023
Available online 31 January 2023

warming, saturated air contains 7% more water vapor, which may lead to an increase in extreme precipitation events if global warming continues unabated (Allen and Ingram, 2002). Both the frequency and intensity of heavy precipitation have increased over China, which is a region particularly vulnerable to extreme precipitation events. The losses resulting from disasters related to heavy precipitation and flooding in China present greater risks as a result of the influence of the East Asian monsoon, the complex topography and large population. The prediction of future changes in extreme precipitation is therefore crucial for both policymakers and the general public and will allow the development of comprehensive adaptation strategies (Zhang and Zhou, 2020).

The ability of climate models to simulate and predict extreme precipitation events is still challenging. Issues such as the quality of the observations, our understanding of physical processes, model biases and internal variability effects all contribute to the uncertainty in projected changes of the regional climate and extreme weather events (Xie et al., 2015; Li et al., 2022). Most models tend to overestimate light precipitation events and underestimate the intensity of heavy precipitation events (Dai, 2006; Sun et al., 2006). Li et al. (2010) found that many low-resolution global models underestimate extreme precipitation by ~50%, especially during summer in East China. Xu et al. (2011) showed that three coupled general circulation models had limited skills in reproducing the interannual variation of extreme precipitation events in the major river basins in East China. Gao et al. (2017) evaluated a high-resolution regional climate model (RegCM4) in simulating heavy precipitation events in East China, which produced substantial underestimates. However, Liang et al. (2019) demonstrated that the CWRF model outperformed the RegCM4.6 model in reproducing extreme precipitation in China. Tripathi and Dominguez (2013) found that spatial structure of the simulation of extreme precipitation by regional climate models at a grid spacing of 10 km was clearer than that at a grid spacing of 50 km in the southwestern US, but there were still large deviations. Prein et al. (2017) indicated that even convection–permitting model (CPM) at a grid spacing of 4 km still underestimates hourly extreme precipitation by up to 30% in the central US during summer. Many research methods have been used to alleviate the “drizzling problem” in models (Xie et al., 2004), but it has been proven difficult to find a perfect solution. The moist physical process performs poorly in most models and will often stimulate wet convection. In nature, the convection inhibition process allows the accumulation of atmospheric instability energy before the beginning of strong convection (Sun et al., 2006).

Previous studies have shown that precipitation is very sensitive to the selection of cumulus parameterization schemes (Huang et al., 2008; Shen et al., 2014, 2016). Convection triggers, entrainment or detrainment equations, closure assumptions and cloud models have been shown to be important factors affecting convective precipitation. Although many studies have discussed the sensitivity and mechanisms of extreme precipitation events due to different physical representations, the simulations and underlying mechanisms of RCM cumulus parameterization schemes over China are still limited. A series of alternative physical parameterization schemes with consistent coupling for each major physical process have been built into the regional Climate–Weather Research and Forecasting (CWRF) model, including cumulus, microphysics, radiation, planetary boundary layer and surface processes (Liang et al., 2012; Li et al., 2020). Zeng et al. (2008) made a 120-h real-time ensemble forecast using eight parameterization combinations in CWRF model and showed that it could produce a good forecast of precipitation in China. Sun and Liang (2020a) found that the simulation of extreme precipitation in the US by CWRF model was significantly better than the reanalysis results of the ERA-Interim (ERI) dataset (Dee et al., 2011). In fact, the simulation results of various parameterization schemes for all kinds of extreme precipitation events in different regions are significantly different.

It is challenging for climate models to comprehensively capture the characteristics of extreme precipitation events and to understand, simulate and predict these events. There is therefore an urgent need to understand and overcome the deficiencies in these models and to investigate the thermal and dynamic processes behind extreme precipitation events. Coumou and Rahmstorf (2012) suggested improving models by increasing their spatial resolution, but it is equally important to strengthen our understanding of the relevant nonlinear processes. Wilcox and Donner (2007) pointed out that it is also crucial to change the convective closure and trigger in the cumulus parameterization formula. Li et al. (2012) showed that their improvements in the simulation of heavy precipitation were mainly a result of the increase in the cloud water path (CWP) and cloud condensation, which are either not included or poorly expressed in conventional convection parameterization. Kang et al. (2015) suggested that the underestimation of extreme precipitation frequency is due to the lack of representation of ice microphysical processes related to heavy precipitation. Zhao and Xu (2020) showed that it is difficult for models to accurately and explicitly analyze entrainment, detrainment and vertical transport processes in the convection process.

Most of the existing studies of extreme precipitation events have focused on the changes and impacts of different parameterization schemes in specific environments, whereas less work has been carried out to explain the underlying physical processes of the model simulation biases based on cumulus convection parameterization schemes. We therefore examined the ability of CWRF model to simulate extreme precipitation events in China using different cumulus parameterization schemes, focusing on three key regions. This study investigates the dependence of extreme precipitation on the different cumulus parameterization schemes and the complex correlation of the factors affecting the biases in extreme precipitation. We established a regression model to explore the underlying physical processes causing the biases in extreme precipitation to provide a reference for further improvements in CWRF model and its applications. The abbreviations of the large number of climate variables used in this paper are summarized in Table S1.

2. Model, experiments, data and methods

2.1. Model and experiments

This study used the regional Climate-Weather Research and Forecasting (CWRF) model, which is a climate extension of the WRF model v3.1.1 (Skamarock et al., 2008). The extension includes numerous improvements about the land-atmosphere-ocean, convection-microphysics, and cloud-aerosol-radiation interactions, as well as the system consistency between the various modules (Liang et al., 2012). The CWRF model has been systematically advanced as a climate extension to the Weather Research and Forecasting model since 2002 by improving the physical process schemes, integrating multiple parameterization schemes and external forcing. The CWRF model not only combines the most advanced conjunctive surface–subsurface processes with the real surface distribution characteristics, but also couples a comprehensive multi-layer upper ocean model and a detailed lake, ice, snow and sediment simulator. In addition, CWRF model integrates a set of alternative parameterization schemes for each key physical process, which are coupled among each component and maintain the greatest consistency. The interaction of the cloud aerosol radiation ensemble system was added to make the physical processes in CWRF model more realistic (Liang et al., 2012).

We used an ensemble cumulus parameterization (ECP) scheme based on the Grell and Dévényi (2002) framework in CWRF model. This scheme not only shows an outstanding performance in the simulation of summer precipitation in the coastal ocean of the US (Qiao and Liang, 2015, 2016, 2017), but also greatly improves the simulation of extreme precipitation over land (Sun and Liang, 2020a, 2020b). The computational domain of CWRF model used in this study was based on the Lambert conformal map projection centered at (35.18° N, 110° E) with a total of 232 (latitude) × 172 (longitude) grid points at 30 km spacing.

There were 36 vertical levels and the top of CWRF model was at 50 hPa.

The simulations were driven by ERI reanalysis dataset as the initial and boundary fields. The simulation began on November 1, 1979 and ran continuously until the end of 2016. We therefore mainly evaluated the results from 1980 to 2016, a total of 37 years, and selected five cumulus parameterization schemes in CWRF model for comparative analysis: ECP (Liang et al., 2012; Qiao and Liang, 2015, 2016, 2017), Kain-Fritsch Eta (KFeta) (Kain and Fritsch, 1993; Kain, 2004), Betts–Miller–Janjic (BMJ) (Betts and Miller, 1986; Janjic, 1994), New Simplified Arakawa–Schubert (NSAS) (Han and Pan, 2011) and Tiedtke (Tiedtke, 1989; Nordeng, 1995) schemes. We then selected a better scheme suitable for simulating extreme precipitation in China and explored the underlying physical processes of the simulation biases. Table S2 summarizes the five cumulus parameterization schemes and gives the main differences in the closure assumptions and trigger functions.

2.2. Data

We used observational data as the reference for model evaluation. These observational data consisted of a set of daily gridded analysis precipitation and temperature at 2 m (T2m) values of CN05.1 dataset (Wu and Gao, 2013). The CN05.1 grid data is derived by interpolating observation data of 2416 stations in mainland China, which has a resolution of 0.25° × 0.25° and has been commonly used in studying extreme precipitation over China (Wu et al., 2015; Wang et al., 2021). We also used the ERI reanalysis data, which assimilated the satellite-retrieved total column water vapor as a pseudo-observation of rainfall in 4D-Var. The ERI data is widely used because it provides one of the best proxies of global gridded observed precipitation spatiotemporal variations (Dee et al., 2011; http://apps.ecmwf.int/datasets/). The precipitation of ERI data provides a reference for CWRF model downscaling skill enhancement due to its driving circulation. In addition, ERI data also implements a variant version of Tiedtke cumulus scheme (Bechtold et al., 2008), which is different from that used in CWRF model.

The National Aeronautical and Space Administration (NASA) Modern-Era Retrospective Analysis for Research and Applications version 2 (MERRA-2) dataset is regarded as a good substitute for observational atmospheric circulation parameters (Rienecker et al., 2011; Molod et al., 2015; Collow et al., 2016; Coy et al., 2016; Reichle et al., 2017; Sun and Liang, 2020b). Previous studies showed that the MERRA-2 reanalysis dataset can well describe the spatiotemporal distribution of precipitation and evolution of the dust aerosols in East Asia (Chen et al., 2019; Zhang, 2019; Yao et al., 2020). Therefore, we used the MERRA-2 reanalysis (including consistent surface and atmospheric conditions) as the reference rather than the driving ERI data (for independence), nor the surface observations (which is disconnected from the circulation). This choice is made for insightful physical understanding, which requires a coupled climate system perspective.

Precipitation and other surface variables of the MERRA-2 data at a horizontal resolution of (0.5° × 0.625°) (https://disc.gsfc.nasa.gov/) were used in our study as a reference proxy for the observational circulation characteristics. Table 1 shows the observational data for the reference as the ground truth, which includes: PR and T2 m from the CN05.1 dataset; CWP from the National Oceanic and Atmospheric Administration (NOAA) Advanced Very High Resolution Radiometer (AVHRR) (https://wui.cmsaf.eu/); and SWD, RSW, OLR and CRE from the long-term NASA/World Climate Research Programme Global Energy and Water Exchanges Surface Radiation Budget (GEWEX-SRB) Integrated Product Release 4.0 (https://gewex-srb.larc.nasa.gov/). The observational and reanalysis data were all interpolated onto the same grid as the CWRF model of 30 km to facilitate comparison. The interpolation method used here is the inverse distance weighting, which is commonly used for climate model evaluation (Li, 2011; Gan et al., 2015). Although the results may differ due to using different interpolation methods, such differences are small (Sun and Liang, 2020a).

Table 1
Observation data used in this study.

Variables	Available time	Sources
Precipitation (PR)	1980–2016	CN05.1(Wu and Gao, 2013)
2 m air temperature (T2M)	1980–2016	
Cloud water path (liquid plus ice) (CWP)	1987–2016	AVHRR(Advanced Very High-Resolution Radiometer,Karlsson et al., 2017)
Shortwave downwelling at surface (SWD)	1984–2010	GEWEX-SRB Integrated Product (Rel-4)(NASA/LARC/SD/ASDC, 2021)
Reflecting solar radiation at top of atmosphere all/clear (RSW)	1984–2010	
Outgoing longwave radiation all/clear (OLR)	1988–2009	
Cloud radiative effect (CRE)	1988–2009	

2.3. Methods

We used the 95th percentile daily precipitation (P95) recommended by the World Meteorological Organization (WMO) to calculate the extreme precipitation index and analyze the climate characteristics of extreme precipitation in different regions and seasons. The P95 is a good indicator that can display key information about the sample distribution without being distorted by abnormal values (Fan et al., 1994). To increase the reliability of P95, we also took into account the number of rainy days (NRD) and the daily rainfall intensity (DRI).

We used Taylor diagrams (Taylor, 2001) and the equitable threat score (ETS) (Gandin and Murphy, 1992) to systematically evaluate the performance of CWRF model simulations. The ETS represents the ratio of the number of events that occur and are simulated correctly to the total number of events after removing random contingencies. The formulas are as follows:

$$ETS = \frac{(H - H_r)}{(H + M + F - H_r)} \tag{1}$$

$$H_r = \frac{(H + M) \times (H + F)}{H + M + F + D} \tag{2}$$

where H is the number of correct precipitation simulations; M is the number of observations, but not simulations; F is the number of simulations, but not observations; D is the situation that there is no precipitation in the observations and simulations; and H_r is the number of possible correct simulations under random conditions. The range of the values of ETS is −1/3 to 1. A zero or negative value of ETS means no simulation skill.

We adopted the concept of component-based analysis to obtain a physical understanding of extreme precipitation simulation biases (Sun and Liang, 2020b), that is, to take into consideration of the meteorological processes by which the basic ingredients are brought together (Doswell et al., 1996). The basic elements required for extreme precipitation events include sufficient supply of water vapor, ascending motion, and precipitation efficiency. These elements may be satisfied in a weather system dominated by deep moist convection. We use variables of RCT, TPW, CAPE, CIN, and W700 to represent the above three basic ingredients. For a deeper understanding of convection-cloud-radiation processes, other relevant variables that may affect extreme precipitation are examined, such as MC, ET, CWP, LFC, LCL, SWD, SH, NSE, PBLH, FCL, FCH, T2M, Q2M, OLR, RSW, CRE, and V850. We first listed the 22 factors that may affect P95 using the component-based method, and then quantitatively analyzed their relationships using the method of all subsets regression (Wasserman and Sudjianto, 1994; Lumley and Miller, 2017) to obtain a concise and effective the multivariable regression models (Alexopoulos, 2010). The multivariable regression model takes the matrix form as:

$$\boldsymbol{Y} = \boldsymbol{XB} + \boldsymbol{\Xi} \tag{3}$$

or in detail as:

$$\begin{pmatrix} y_1 \\ y_2 \\ y_3 \\ \vdots \\ y_n \end{pmatrix} = \begin{pmatrix} 1\ x_{11}\ x_{12} \cdots x_{1q} \\ 1\ x_{21}\ x_{22} \cdots x_{2q} \\ 1\ x_{31}\ x_{32} \cdots x_{3q} \\ \vdots\ \vdots\ \vdots \ddots\ \vdots \\ 1\ x_{\mathrm{n1}}\ x_{\mathrm{n2}} \cdots x_{\mathrm{nq}} \end{pmatrix} \begin{pmatrix} \beta_0 \\ \beta_2 \\ \beta_3 \\ \vdots \\ \beta_q \end{pmatrix} + \begin{pmatrix} \epsilon_1 \\ \epsilon_2 \\ \epsilon_3 \\ \vdots \\ \epsilon_n \end{pmatrix} \tag{4}$$

where $\boldsymbol{Y}$ is the n matrix of the predicted value of P95; $\boldsymbol{X}$ is the $n \times (1+q)$ matrix of the variables that may affect P95 (including RCT, TPW, CAPE, CIN, W700, MC, ET, CWP, LFC, LCL, SWD, SH, NSE, PBLH, FCL, FCH, T2M, Q2M, OLR, RSW, CRE, and V850); $\boldsymbol{B}$ is the $(q+1)$ matrix of the regression coefficients; $\boldsymbol{\Xi}$ is the n matrix of the regression model residual error. Table S1 summarizes the abbreviations and definitions of these 22 factors. The correlations were considered as statistically significant if they passed Student's *t*-test at the 95% confidence level.

3. Results

3.1. Distribution of seasonal average and extreme precipitation in China

Fig. 1 compares the spatial distribution of the seasonal average precipitation over a 37-year period (1980–2016) in observations, ERI reanalysis data and simulations (from the control experiment of CWRF model using ECP scheme). Winter (Fig. 1a, e, i) is a dry season in China when the total precipitation is <5 mm/day, mainly distributed in the Yangtze and Pearl River basins to the east of 110° E. The ERI data and CWRF model capture this feature well, but ERI data (CWRF model) systematically underestimates (overestimates) the precipitation intensity in this region.

In spring (Fig. 1b, f, j), the observational data show two centers of precipitation south of the Yangtze River and north of the Pearl River. The ERI data and CWRF model capture these centers well, although CWRF model slightly overestimates the precipitation. The CWRF model also overestimates the precipitation near the Changbai Mountains in northeast China (see Fig.S1), where the observed precipitation is <2 mm/day.

In summer (Fig. 1c, g, k), the observational data show two rain bands in the Yangtze River basin and across South China, whereas the rain band structures in ERI data are smoother and wider than those in the observations. By contrast, CWRF model shows the fine structures of the two rain bands, but one rain band along the Yangtze River basin is weak, whereas the other rain band in the coastal areas of South China is strong. The CWRF model generally underestimates precipitation over the area between the two rain bands. The summer rainfall over the Greater Hinggan Mountains, the Lesser Hinggan Mountains and the Changbai Mountains (see Fig.S1) of the Northeast Plain is intense. The ERI data reproduces this feature well, whereas CWRF model slightly overestimates the rainfall. Liang et al. (2019) reported that the intensity of precipitation over mountains is underestimated by the observational data because there are few observational stations in these areas, with most stations located at low altitudes.

Autumn (Fig. 1d, h, l) is the transitional season between the summer and winter monsoons in China. The observational data show that precipitation is distributed evenly and there is a weak center of precipitation in the Yangtze River basin. The CWRF model captures these characteristics better than ERI data, but underestimates the intensity of precipitation. The simulation of the seasonal average precipitation shows the added value of the more comprehensive physical configuration and higher resolution of CWRF model, which captures finer characteristics of the regional precipitation in China than ERI data.

Fig. 2 shows the distributions of the seasonal average NRD during the time period 1980–2016. In all seasons, CWRF model captures a finer

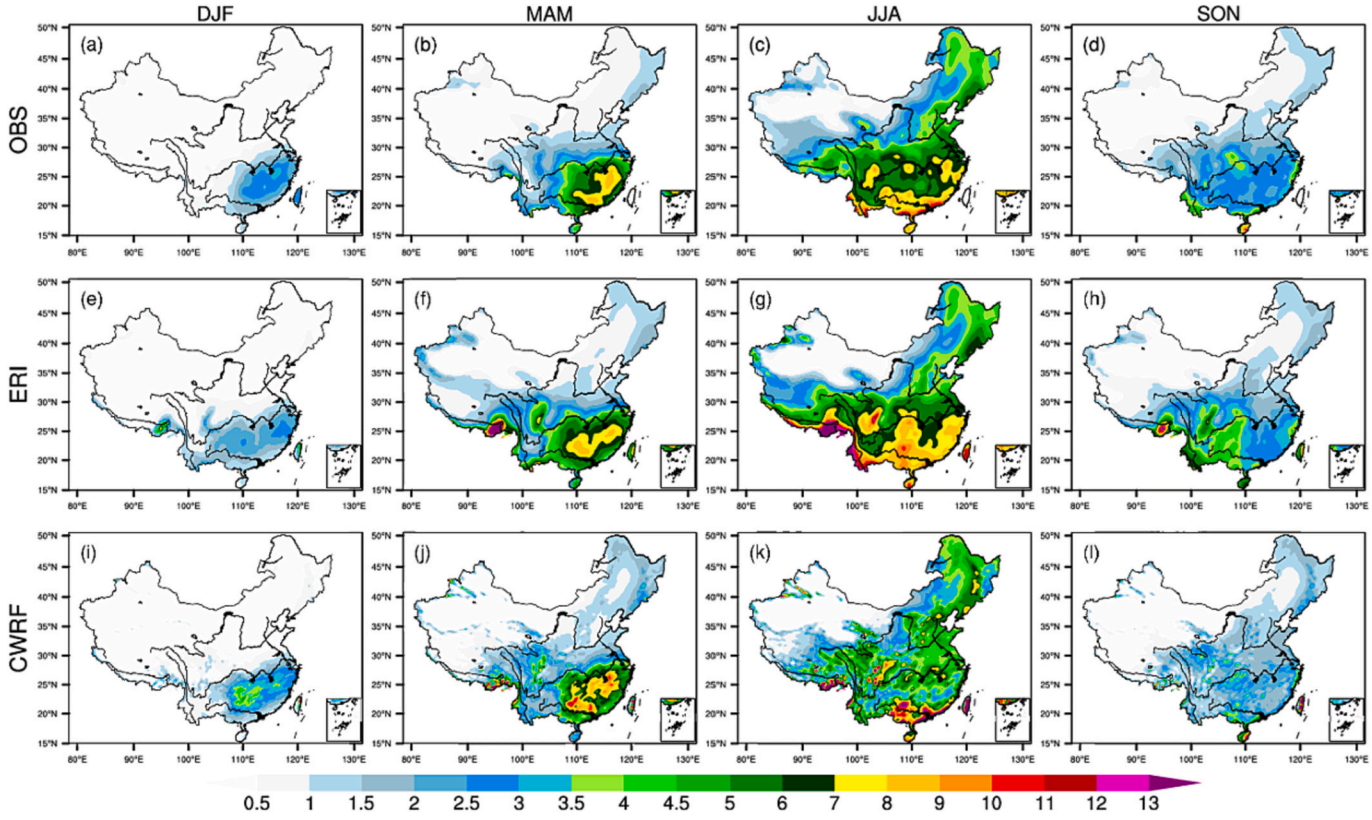

Fig. 1. (a, e, i) Winter, (b, f, j) spring, (c, g, k) summer and (d, h, l) autumn average precipitation (units: mm/day) of (a–d) observations, (e–h) ERI reanalysis dataset and (i–l) CWRF simulation with ECP scheme during the time period 1980–2016.

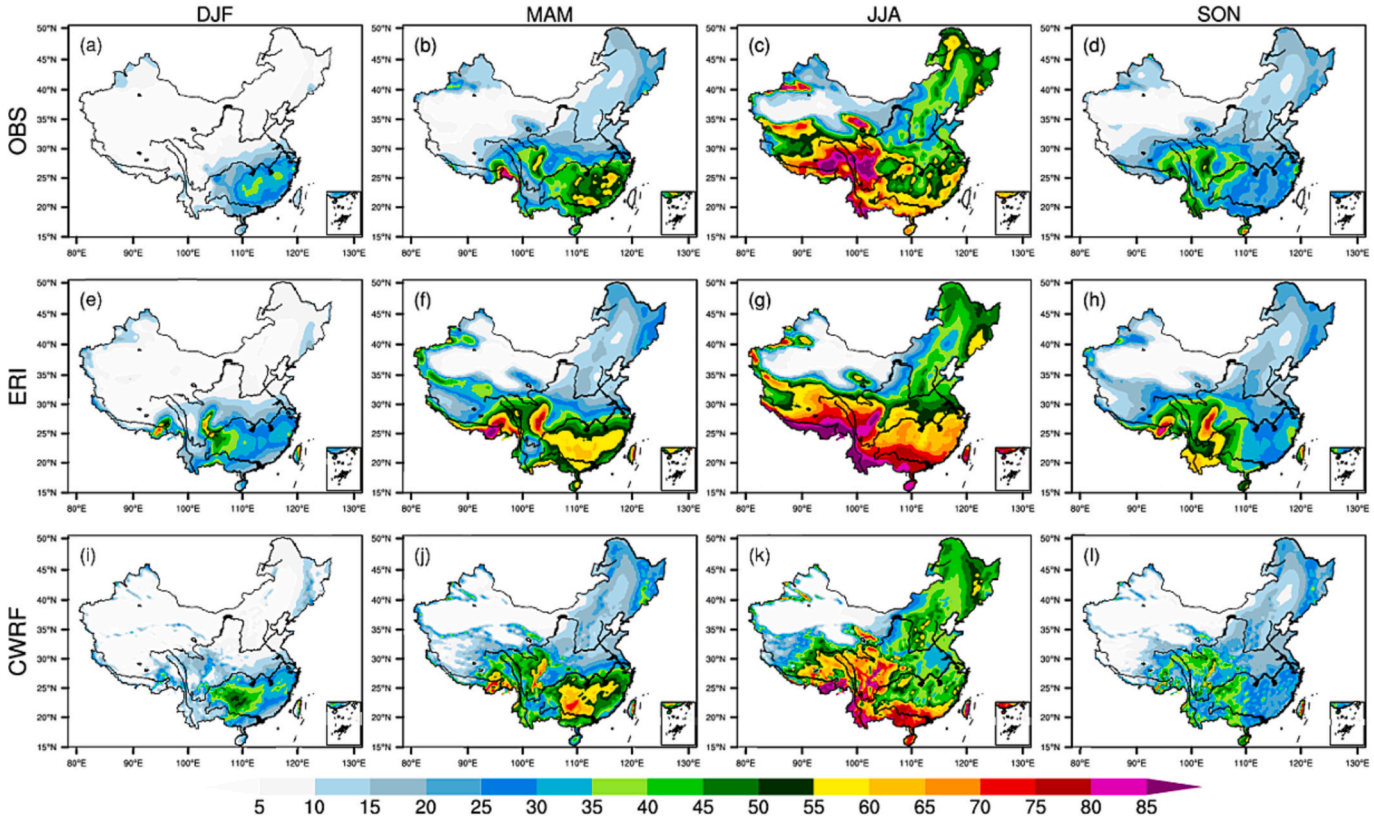

Fig. 2. (a, e, i) Winter, (b, f, j) spring, (c, g, k) summer and (d, h, l) autumn average NRD (units: days) in (a–d) observations, (e–h) ERI reanalysis dataset and (i–l) CWRF simulation with ECP scheme during the time period 1980–2016.

structure of the distribution of NRD in the observations than ERI data, especially in southwest China. In winter (Fig. 2a, e, i), both ERI data and CWRF model show the peak values of NRD between the Yangtze and Pearl River basins, but the center of the maximum value shifts to the southwest relative to the observations. In spring (Fig. 2b, f, j), CWRF model reproduces more of the characteristics of the spatial pattern of NRD than ERI data, but the location of the large-value center shifts to the west. In summer (Fig. 2c, g, k), ERI data generally overestimates NRD in the southern Yellow River basin. Sun and Liang (2020a) reported that ERI data compensated for weak precipitation intensities by simulating more rainy days to produce a more reasonable total precipitation, a typical "drizzling problem" in GCMs, but that CWRF model could effectively reduce this overestimation. By contrast, CWRF model overestimates NRD in Guangdong and Guangxi and underestimates NRD on the Yunnan–Guizhou Plateau and the southern foothills of the Qinghai–Tibetan Plateau. The CWRF model has a greater uncertainty in simulations of precipitation in southwest China because the resolution is too low to accurately describe the steep terrain in this region. In autumn (Fig. 2d, h, l), ERI data overestimate NRD in the southeastern Qinghai–Tibetan Plateau, whereas CWRF model has a relatively high simulation skill. The CWRF model therefore has a stronger ability to simulate NRD, which improves ERI simulation of NRD in China.

Fig. 3 shows the spatial distributions of the seasonal average extreme precipitation (P95) in observations, ERI data and CWRF simulation. The CWRF model outperforms ERI data in all seasons in North and South China and in the mid- to lower reaches of the Yangtze River. The ERI data clearly underestimate the peak value of P95, especially in the coastal areas of South China. The CWRF model produces more details of the spatial distribution of P95, so it could truly capture any changes. In winter (Fig. 3a, e, i), CWRF model accurately describes the magnitude and range of P95, whereas ERI data significantly underestimate the peak value of P95. In spring (Fig. 3b, f, j), the observations show that P95 decreases from southeast to northwest. The ERI data underestimate P95 in the coastal areas south of the Yangtze River, whereas CWRF model captures this characteristic. In summer (Fig. 3c, g, k), there is heavy precipitation (>30 mm/day) in a large part of East China, with maximum precipitation (>40 mm/day) in the Yangtze River basin. The ERI data systematically underestimate P95, especially in southeast China, and roughly capture the center of P95 along the Yangtze River, although the center shifts to the south. The CWRF model reproduces the central position and size of P95 rain bands along the Yangtze and Pearl River basins. The rain bands over the three mountain ranges (the Greater and Lesser Hinggan Mountains and the Changbai Mountains) in the Northeast Plain simulated by CWRF model are stronger than in observations. Because the observation stations are sparsely distributed, the distributions of precipitation presented by CN05.1 observational data have little reference significance.

The distributions of P95 in autumn (Fig. 3d, h, l) are similar to those in summer, but with a weaker intensity. The observations show that the maximum along the Yangtze River is close to 25 mm/day, which is also visible and more dispersed in CWRF simulation, but decreases in ERI data. Another characteristic is the heavy rain band in the coastal area of South China; CWRF model distinguishes the increase in precipitation caused by coastal sea breezes better than ERI data (Liang et al., 2019).

3.2. *Sensitivity of extreme precipitation simulation to cumulus parameterization*

Clearly, regional differences exist in the changes of extreme precipitation across China due to monsoons and geographical environment. Referring to Liang et al. (2019) for the classification of distinct climate regimes, we selected three key regions: North, Central and South China, where extreme precipitation events are significant, especially in summer (Fig. 3a, b, c, d). Over these regions, observations are more reliable due

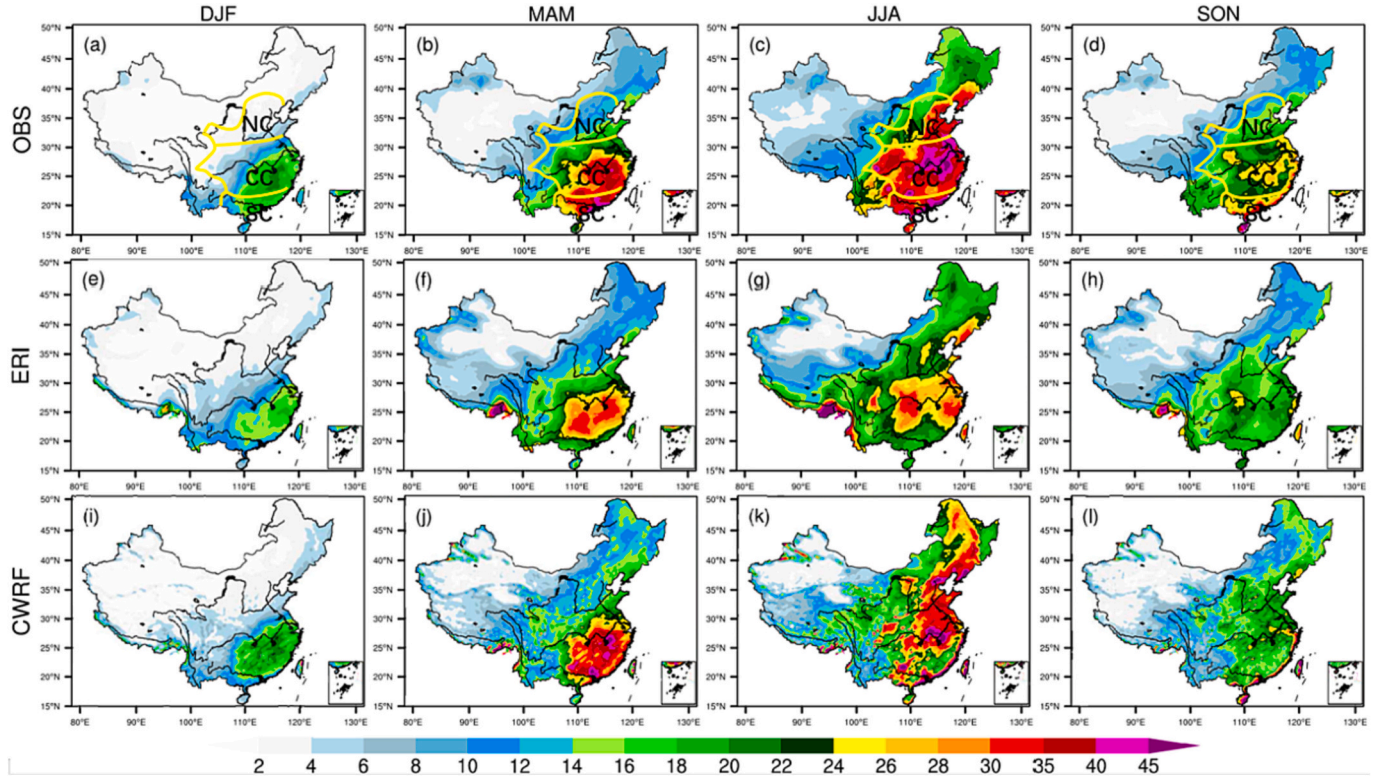

Fig. 3. (a, e, i) Winter, (b, f, j) spring, (c, g, k) summer and (d, h, l) autumn average P95 (units: mm/day) of (a–d) observations, (e–h) ERI reanalysis data and (i–l) CWRF simulation with ECP scheme during the time period 1980–2016. Shading represents P95; yellow curves represent the geographical location of North China (NC), Central China (CC) and South China (SC). (For interpretation of the references to colour in this figure legend, the reader is referred to the web version of this article.)

to dense monitoring sites and small topographic influences; also, the CWRF well captures the observed extreme precipitation characteristics, both of which provide creditability for understanding regional processes. Hence the advantage of CWRF model may be that the results improve the physical parameterizations of the model at high resolution (Sun and Liang, 2020a). This downscaling skill provides a unique opportunity to explore the sensitivity of P95 simulation to the various cumulus parameterization schemes in CWRF model. This paper mainly discusses the regions of North, Central and South China and compares P95 simulation effects of five of the cumulus parameterization schemes in CWRF model in detail.

Fig. 4 compares the spatial distributions of the seasonal average P95 biases of ERI data and CWRF simulations with the different cumulus parameterization schemes. In winter (Fig. 4a, e, i, m, q, u), the simulation biases of the cumulus parameterization schemes are small, apart from BMJ scheme, which substantially underestimates P95 bias in Central China to the east of 110° E. In spring (Fig. 4b, f, j, n, r, v), the underestimated area of BMJ scheme expands further and KFeta and Tiedtke schemes overestimate P95 biases in Central China. The ERI data and NSAS schemes are unable to simulate the maximum rain band of P95 along the coastline of South China. By contrast, in winter and spring, P95 intensity simulated by CWRF model with ECP scheme is the closest to observations.

In summer (Fig. 4c, g, k, o, s, w), Tiedtke scheme overestimates P95 in North China by >20 mm/day and KFeta scheme overestimates P95 in Central China to the east of 110° E by >20 mm/day. However, Tiedtke scheme improves P95 overestimation of KFeta scheme in South China. The ERI data and BMJ scheme substantially underestimate P95 by 5–10 mm/day in the coastal areas of North China and the mid- to lower reaches of the Yangtze and Pearl River basins. By contrast, the bias distributions of P95 simulated by ECP and NSAS schemes are similar. In Central and South China, the negative bias range (−15 to −5 mm/day) of NSAS scheme is smaller than that of ECP scheme. In autumn (Fig. 4d, h, l, p, t, x), the distributions of bias are similar to those in summer, but the range and magnitude of the biases are smaller than those in summer.

These results show that ECP scheme generally reproduces the distribution of observed P95. The ECP scheme is developed from the Grell-3 ensemble cumulus parameterization (G3; Grell and Dévényi, 2002) with many improvements including the selection and weighting of closure assumptions that are specific of land or oceans. Using the assumptions of the land moisture convergence closure and oceanic large-scale cloud base vertical velocity (Qiao and Liang, 2015, 2016, 2017), it can deal with comparisons between ocean and land more comprehensively and generates sufficient convective activity, which helps to capture the occurrence of extreme precipitation events and greatly improves the deficiencies in ERI simulations.

Fig. 5 compares the spatial distributions of the seasonal average biases of NRD in ERI data and CWRF simulations with different cumulus parameterization schemes. In winter and spring, all the schemes overestimate NRD by 10–25 days in North China to the east of 110° E. In addition, the negative NRD bias of Tiedtke scheme is the largest of all schemes in North China and the coastal areas of South China in spring. The BMJ scheme overestimates NRD by 5–10 days in North China. In summer (Fig. 5c, g, k, o, s, w), Tiedtke scheme substantially underestimates NRD in North, Central and South China, and, in particular, underestimates NRD by >35 days in the coastal areas of Central and South China. The BMJ scheme substantially underestimates NRD in the Yangtze River basin, which is consistent with the result that the simulated P95 has a large negative bias. The performance of KFeta and NSAS schemes are similar, especially in coastal areas, with an underestimation of NRD by 5–10 days. The ECP scheme has a small negative bias in Central China and a positive bias of 5–10 days in North and South China. Interestingly, only ERI data significantly overestimate NRD by 5–15 days in North, Central and South China. In autumn (Fig. 5d, h, l, p, t, x),

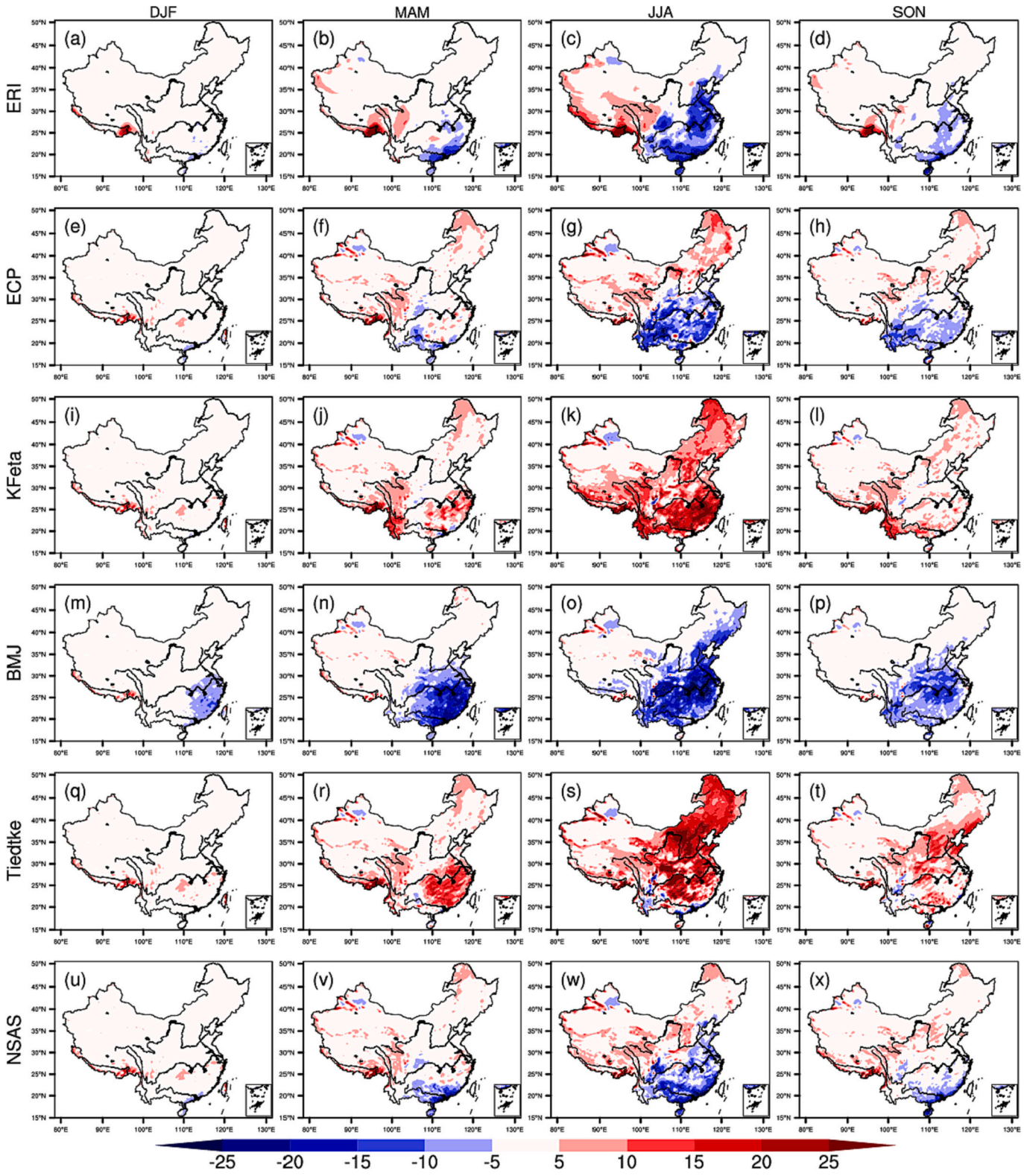

Fig. 4. (a, e, i, m, q, u) Winter, (b, f, j, n, r, v) spring, (c, g, k, o, s, w) summer and (d, h, i, p, t, x) autumn average P95 daily precipitation biases (units: mm/day) of (a–d) the ERI reanalysis data and the CWRF simulations using the (e–h) ECP, (i–l) KFeta, (m–p) BMJ, (q–t) Tiedtke and (u–x) NSAS cumulus parameterization schemes during the time period 1980–2016.

ERI data and the CWRF simulations of all schemes perform good in these three regions, with only small biases.

The daily precipitation intensity (DRI) biases of ERI reanalysis data and CWRF simulations with different cumulus parameterization schemes (see Fig. S2) are highly correlated with P95 biases (Fig. 4) in all seasons. We calculated the spatial pattern correlation coefficient (PCC) between DRI biases and P95 biases in China (Table 2). The correlations in all seasons apart from winter are all >0.92 and the annual average correlation coefficients of all schemes are >0.93. The high correlation between DRI biases and P95 biases indicate that the underestimations of

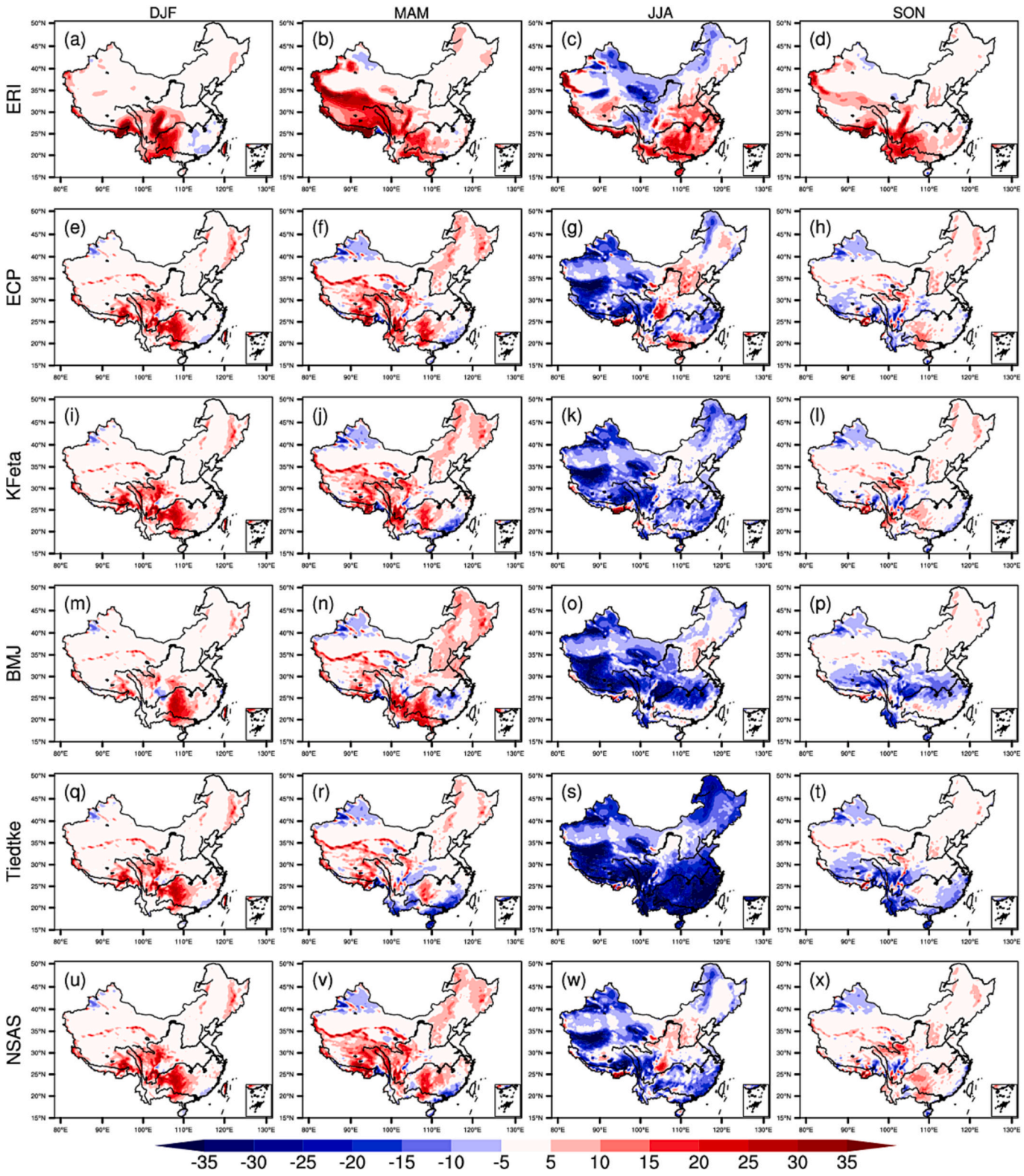

Fig. 5. (a, e, i, m, q, u) Winter, (b, f, j, n, r, v) spring, (c, g, k, o, s, w) summer and (d, h, i, p, t, x) autumn average NRD (units: days) biases of (a–d) the ERI reanalysis data and the CWRF simulations using the (e–h) ECP, (i–l) KFeta, (m–p) BMJ, (q–t) Tiedtke and (u–x) NSAS cumulus parameterization schemes during the time period 1980–2016.

extreme precipitation occur as a result of the systematic decrease in the precipitation intensity, whereas the overestimations of extreme precipitation occur as a result of the systematic increase in precipitation intensity. This explains the important relationship between extreme precipitation and precipitation intensity, especially the simulation results of KFeta and BMJ schemes.

Based on the simulated P95 biases, we divided the cumulus schemes into three broad types. The first type includes KFeta and Tiedtke schemes, which substantially overestimate P95 in the three regions. The second type produces a significant underestimation in three regions (e.

Table 2
Spatial pattern correlation coefficients between DRI biases and P95 biases over China during the time period 1980–2016.

Season	Scheme					
	ERI	ECP	KFeta	BMJ	Tiedtke	NSAS
DJF	0.89	0.89	0.90	0.93	0.89	0.90
MAM	0.95	0.95	0.97	0.97	0.96	0.95
JJA	0.95	0.93	0.97	0.95	0.92	0.95
SON	0.92	0.95	0.96	0.95	0.94	0.96

g., BMJ scheme). The third type of cumulus parameterization scheme overestimates P95 in North China and underestimates P95 in Central and South China (e.g., ECP and NSAS schemes).

The PCC and standard deviation of extreme precipitation (P95) in the ERI reanalysis data and CWRF simulation relative to observations are calculated for North, Central and South China using Taylor (2001) diagrams (Fig. 6). The azimuth represents the PCC between the observations and simulations and the polar radius represents the standard deviation of the observations and simulations. In North China (Fig. 6a, d, g, j), the correlation coefficient between the ERI reanalysis data and the observational P95 in summer is lowest (0.42) and the standard deviation is substantially underestimated (0.35). The correlations in other seasons (0.92 in winter, 0.8 in spring and 0.7 in autumn) are higher than in summer, but the standard deviations are still significantly underestimated (0.6–0.8). In winter, the PCCs of P95 between the CWRF simulations and the observations are very close (0.85–0.92) and the standard deviations are underestimated (0.60–0.95); the standard deviation of Tiedtke scheme is the closest to 1.0. In spring, the PCCs (0.63–0.78) between the simulated and observed P95 are lower than that (0.8) between ERI data and the observations; the correlation of NSAS scheme is the highest (0.78) and that of BMJ scheme is the lowest (0.6). In particular, ECP scheme shows the smallest fluctuation in P95 simulation bias (0.84). In summer, the CWRF simulation performance for P95 is higher than that of ERI data. The simulation effect of KFeta scheme is the best, with the highest PCC (0.82), followed by ECP scheme (0.73). The bias fluctuation is smallest for the simulation (1.02–1.04). KFeta scheme performs the best in autumn. However, Tiedtke scheme substantially overestimates the standard deviations in summer (1.4) and autumn (1.5).

In Central China (Fig. 6b, e, h, k), the PCCs between the simulation of P95 using ECP, KFeta and Tiedtke schemes and the observations in winter are as high as 0.95 (0.95, 0.95 and 0.96, respectively), although the smallest simulation bias fluctuation is for ECP scheme (1.04). The PCC of P95 between ECP scheme and observations reaches a maximum in spring (0.9), summer (0.65) and autumn (0.68), but overestimates the standard deviations in summer (1.5) and autumn (1.3). In spring, KFeta and Tiedtke schemes better simulate the spatial pattern of P95 (PCC 0.89), but produce large standard deviations of 1.4 and 1.65, respectively. In summer, KFeta and Tiedtke schemes also substantially overestimate P95 biases in Central China (Fig. 4) and they have abnormally high standard deviations, even beyond the scope of the Taylor diagram. In autumn, the simulation skill of KFeta scheme is similar to that of ECP scheme; they almost coincide in the Taylor diagram. By contrast, BMJ scheme has the poorest skill in all seasons in Central China, with the lowest correlation, especially in summer. In Central China, ECP scheme has the best performance in simulating the spatial pattern of P95 in winter and spring.

In South China (Fig. 6c, f, i, l), the simulated P95 distributions of CWRF model with various cumulus schemes are better than ERI data in all seasons. In winter, KFeta scheme has the highest PCC (0.85) and the standard deviation is the closest to 1.0. In spring, ECP scheme gives the best simulation of P95. Although the standard deviation (1.4) is relatively large, the PCC is the highest (0.82). The PCCs of the simulations with KFeta, BMJ and NSAS schemes are <0.7 (ranging from 0.2 to 0.6). In summer, the simulations of KFeta and Tiedtke schemes are beyond the range of the diagram as outliers and the standard deviation (1.8) of P95 simulated by ECP scheme is large, similar to the situation in Central China. BMJ scheme has the highest PCC (0.68) and the smallest standard deviation (1.2) in summer, but it substantially underestimates the magnitude of P95 in South China (Fig. 4). It is hard to convince that the result of the univariate simulation P95 of BMJ scheme is better than other schemes, which is probably the appearance of some wrong synthesis of BMJ scheme. BMJ scheme has a better simulation skill than the other schemes in summer, but requires a lot of simulations and comparisons with multiple variables in addition to P95. In autumn, the PCCs between the simulated P95 of ECP and KFeta schemes and the observations are 0.77 and 0.70, respectively, but the standard deviation of ECP scheme (1.4) is higher than that of KFeta (1.1) scheme. NSAS scheme gives a poor simulation of P95 in summer and autumn.

We used ETS to examine the simulation performance for P95. Based on the range of observed P95 in each season, ETS is calculated using the number of times that the simulation value hits or misses the range of observed values. Fig. 7 compares ETS at a bin interval of 1.0 mm/day for the 37-year average P95 distribution in each season between the ERI reanalysis data and the CWRF simulations with various cumulus schemes in North, Central and South China. In general, the ETS values of both ERI data and CWRF model in the cold seasons (winter and spring) are higher than those in the warm seasons (summer and autumn), which indicates that it is more complex and difficult to simulate extreme precipitation in the warm seasons.

In North China (Fig. 7a, d, g, j), ERI data and CWRF model only capture the ETS of light rain $\geq$1.5 mm/day in winter, which may be limited by the description of the observational reference data. The ETS of light rain (1.5–10 mm/day) is lowest in ECP scheme and the maximum score is only 0.5. The maximum ETS of ERI data and the other schemes are >0.7 and the maximum ETS of ERI data for a daily precipitation of 9 mm/day reached 0.9. The ETS of BMJ scheme is low in spring, but the ETS of ERI data and other schemes for moderate rain (10–20 mm/day) in spring is 0.5. In summer, the ETS of ERI data is better than those of CWRF simulations in the range 12–25 mm/day. By contrast, when the daily precipitation is >25 mm/day, the ETS of ERI data is almost zero. ECP scheme significantly improves P95 simulation, with an ETS >0.6, significantly higher than the other schemes. The ETS of ECP is the highest (about 0.4) in the daily precipitation range 7–13 mm/day in autumn, but the score is lower than that for ERI data in the range 13–20 mm/day. Apart from ECP scheme, ETS is usually low when CWRF model uses other cumulus parameterization schemes.

In Central China (Fig. 7b, e, h, k), the values of ETS are highest in winter (up to 0.8) and lowest in summer (up to 0.2), which highlights the difficulty of simulating extreme events in summer. In winter, the ETS (>0.7) of all the schemes, apart from BMJ scheme, for the whole P95 range is higher than those of ERI data. In particular, the ability of the low-resolution ERI data to capture low-level light rains (2.0–10 mm/day) is lower than that of the high-resolution CWRF model. The ETS of ECP scheme is the highest (about 0.8) in the daily precipitation range 5–17 mm/day.

ECP scheme shows high skills in simulating daily precipitation >25 mm/day in spring, summer and autumn, with ETS values of 0.7, 0.2 and 0.3, respectively. KFeta and Tiedtke schemes substantially overestimate P95 in Central China (Fig. 4), but it can be seen from Fig. 7 that these two schemes improve the simulation of light and moderate rain <25 mm/day from spring to autumn. After replacing ECP scheme with KFeta and Tiedtke schemes, CWRF simulation systematically improves ETS in spring, summer and autumn, respectively, up to 0.6, 0.1 and 0.5. In summer and autumn, the CWRF cumulus parameterization schemes mostly have high simulation scores with precipitation >25 mm/day, but ERI data have completely missed this and have almost no score. BMJ scheme substantially underestimates P95 in Central China (Fig. 4), so ETS in all seasons is the lowest and there is almost no simulation skill in summer (ETS close to 0).

In South China (Fig. 7c, f, i, l), over the entire P95 range, the

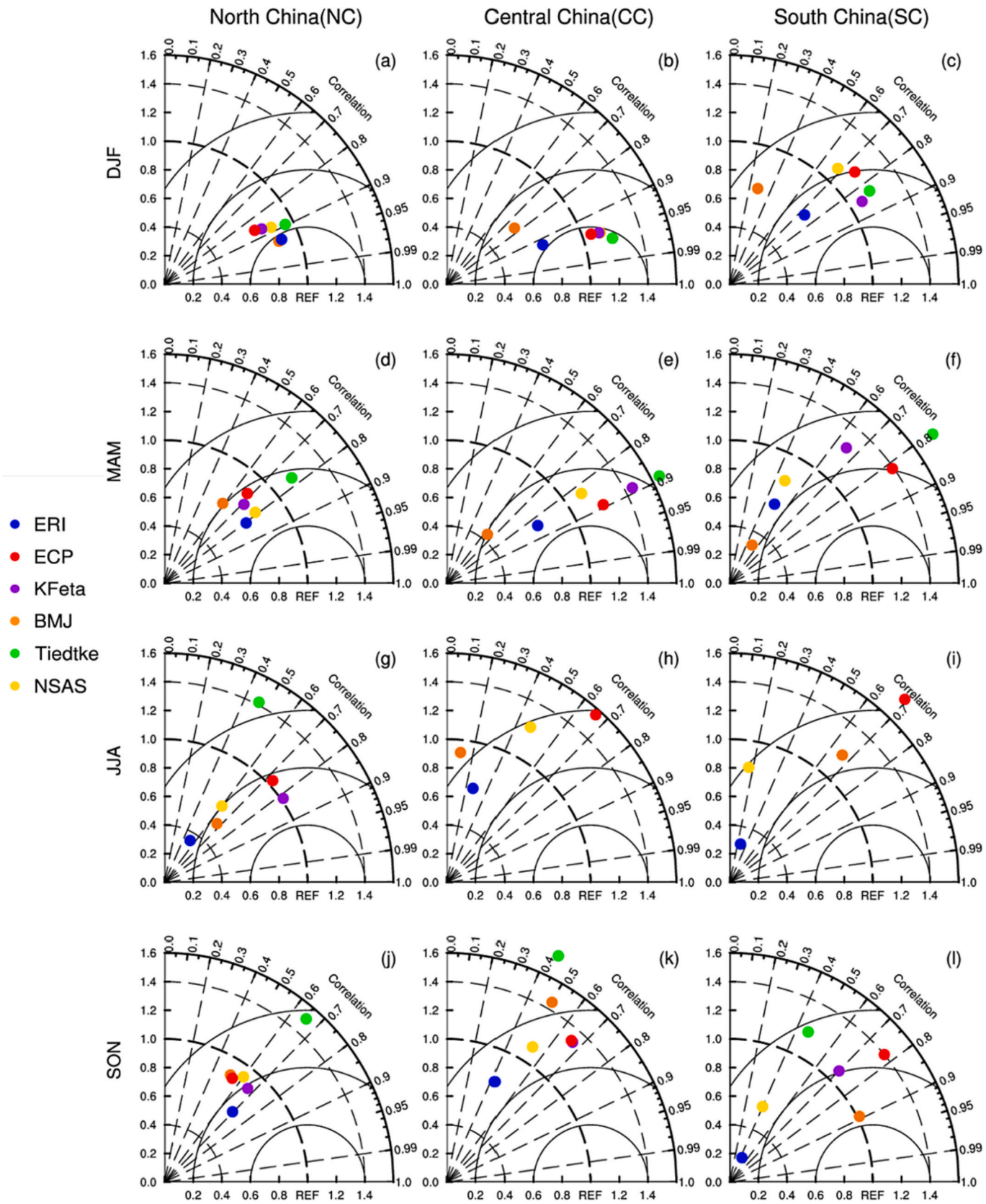

Fig. 6. Taylor diagram of the pattern statistics comparing the overall performance among ERI data and all CWRF cumulus parameterization schemes in simulating the seasonally averaged geographical distribution of P95 during the time period 1980–2016 over (a, d, g, j) North China, (b, e, h, k) Central China and (c, f, i, l) South China in (a, b, c) winter, (d, e, f) spring, (g, h, i) summer and (j, k, l) autumn. The azimuth and radius represent the PCC and the standard deviation with the observations, respectively. REF (OBS) marks the perfect score with a unit correlation and deviation. Poorly performing outliers are off the chart.

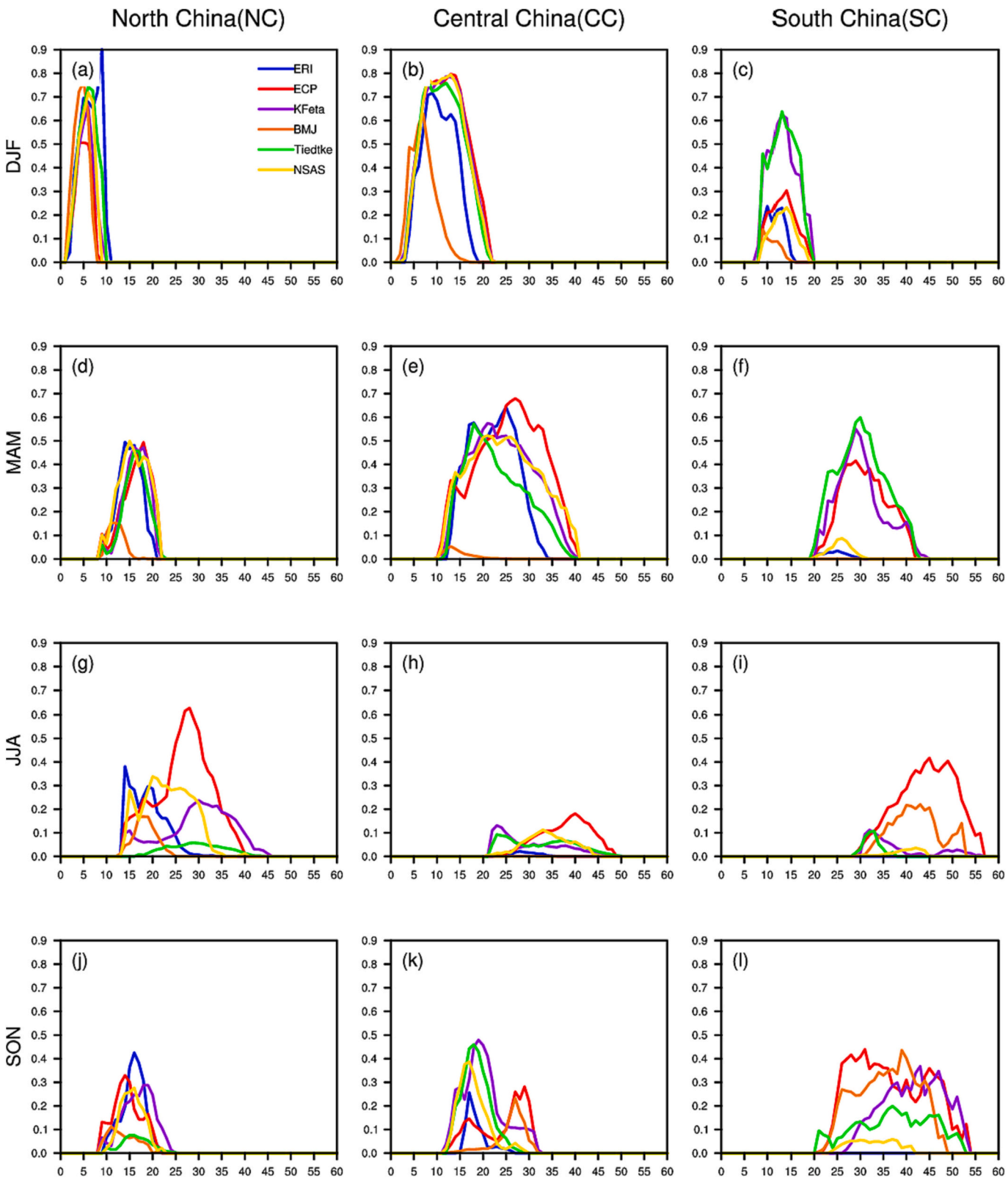

Fig. 7. The ETS of the 1980–2016 seasonally averaged P95 for ERI data and CWRF model with various cumulus parameterization schemes over (a, d, g, j) North China, (b, e, h, k) Central China and (v, f, i, l) South China in (a, b, c) winter, (d, e, f) spring, (g, h, i) summer and (j, k, l) autumn. The *x*-axis represents the P95 threshold at a bin interval of 1 mm/day; the *y*-axis represents ETS values.

simulation skills of CWRF model with all cumulus schemes are significantly better than those of ERI data. The ETS of ERI data is almost zero in all seasons apart from winter. In the cold seasons (winter and spring), Tiedtke and KFeta schemes score higher (>0.4) over the entire P95 range and ECP scheme falls behind these two schemes. However, Tiedtke and KFeta schemes perform poorly in the warm seasons and their ETS is ≤0.2. In summer, the ETS of ECP scheme reaches 0.4 (40–50 mm/day), which is higher than other schemes and ERI data. In autumn, ECP scheme has a high score for daily precipitation of 25–35 mm/day, but this decreases above 35 mm/day. The simulation skill of BMJ scheme only has a high ETS (maximum 0.4) within the range 25–45 mm/day in autumn. NSAS scheme has the lowest ETS in all seasons in South China. It is >0.1 in winter, but the simulation skills in other seasons are very poor (<0.1).

Five cumulus parameterization schemes produce large CWRF discrepancies in simulating extreme precipitation characteristics over three regions. In general, the ECP scheme simulates more realistic extreme precipitation characteristics over all three regions than the other schemes. The ECP combines five major closures with various weights separating land and ocean to more reasonably determine the cloud base mass flux (Qiao and Liang, 2015, 2016, 2017). The KFeta and Tiedtke schemes both generate excessive extreme precipitation as they adopt the closure that assumes the total convective available potential energy (CAPE) is completely exhausted for rainout. The BMJ and NSAS schemes are based on the quasi-equilibrium closure assumption. While the BMJ scheme substantially underestimates extreme precipitation, the NSAS

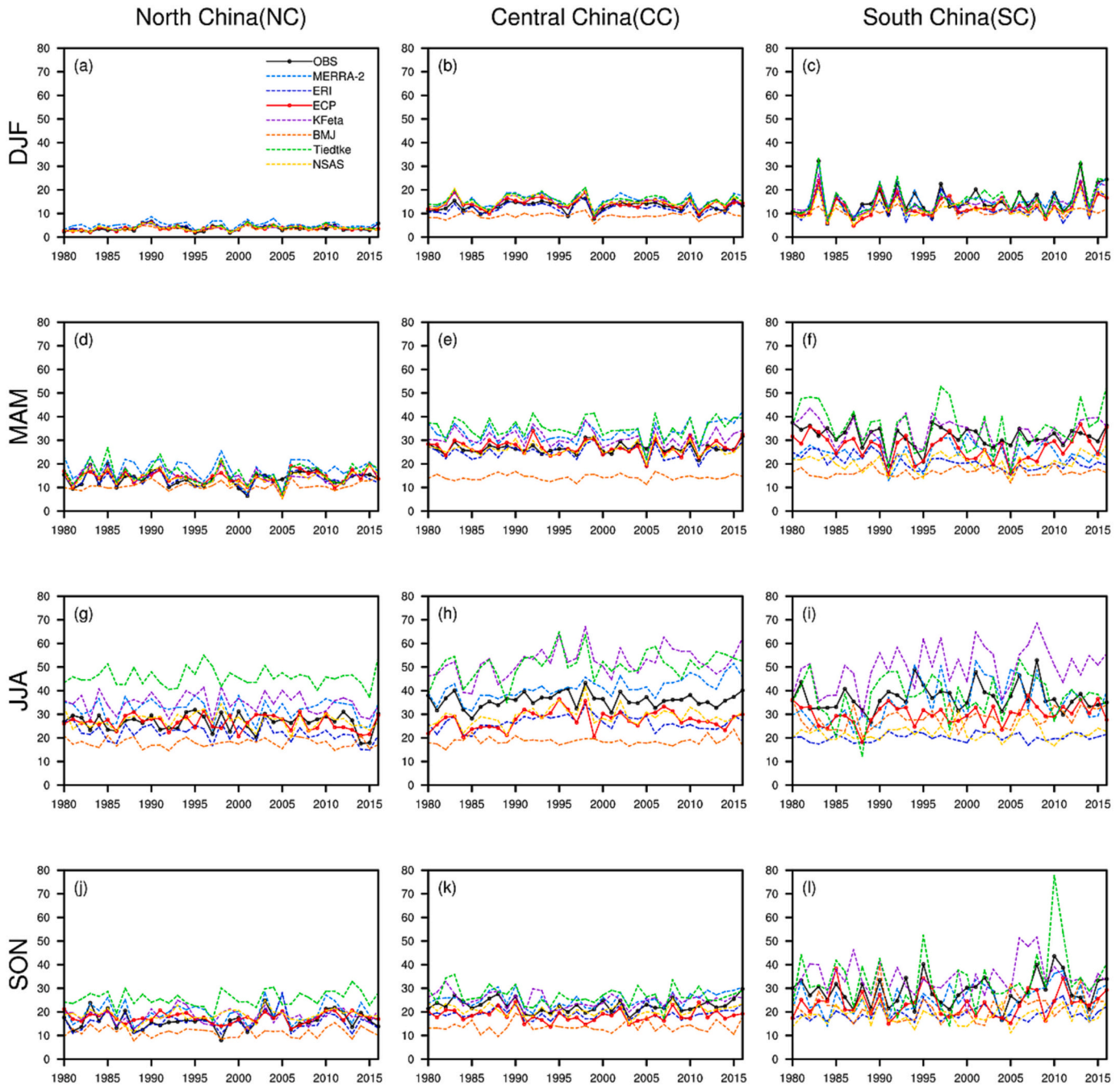

Fig. 8. Time series of seasonally averaged P95 over (a, d, g, j) North China, (b, e, h, k) Central China and (c, f, i, l) South China in observations (OBS), reanalysis data (ERI and MERRA-2) and simulation (CWRF model with ECP, KFeta, BMJ, Tiedtke, and NSAS cumulus parameterization schemes) for (a–c) winter, (d–f) spring, (g–i) summer, and (j–l) autumn for the time period 1980–2016.

scheme performs better because it incorporates improved trigger functions to produce more convection in large-scale convergence regions and less convection in subsidence regions (Han and Pan, 2011).

3.3. Dependence of P95 simulation on cumulus parameterization

Our analyses show that CWRF model significantly improves the simulation of the spatial distributions of P95 in China compared with ERI data. We explored the underlying physical processes of the cumulus parameterization scheme for CWRF model to simulate P95 by comparing the long-term integration of CWRF model with ERI data. Referring to the research methods of Sun and Liang (2020b), we used MERRA-2 reanalysis dataset as a reference, which may help to improve our understanding of the physical processes of the simulated P95 departures.

Fig. 8 compares the interannual variation of P95 in North, Central and South China in all four seasons in the time period 1980–2016 for observations, MERRA-2, ERI and CWRF simulations of varying cumulus schemes. Fig. 9 shows their temporal correlation coefficient (TCC) and root-mean-square error (RMSE) compared with the observational data. In North China (Fig. 8a, d, g, j and Fig. 9a), ECP and NSAS schemes depict the interannual variation of P95 with relatively high TCCs (0.74 and 0.72 in winter; 0.78 and 0.82 in spring) and small RMSEs (0.82 and 0.95 in winter; 2.13 and 1.77 in spring). The ERI data represent P95 most realistically, with the highest TCCs (0.94 and 0.96) and the smallest RMSEs (0.75 and 1.20) in winter and spring, respectively. In summer and autumn, the interannual variation of P95 in MERRA-2 dataset has the highest TCCs (0.93 and 0.90, respectively), followed by ERI data (0.82 and 0.80, respectively), whereas the RMSEs (6.37 and 4.33, respectively) of MERRA-2 dataset are slightly higher than those of ERI data (5.14 and 2.86, respectively) as a result of the overestimation of P95 magnitude in MERRA-2 dataset. The TCCs of the CWRF-simulated P95 are not as good as those of ERI data in summer and autumn. KFeta scheme in summer and BMJ scheme in autumn have the highest TCCs (0.82 and 0.58, respectively) for the simulation of the interannual variation of P95, but the RMSEs (8.82 and 5.79, respectively) are large as a result of the serious overestimation of the interannual variation of P95 by KFeta scheme and its underestimation by BMJ scheme. In summary, the various cumulus parameterization schemes of CWRF model cannot simulate the interannual variation of P95 in North China well and require further improvement.

In Central China (Fig. 8b, e, h, k and Fig. 9b), except in autumn, the TCCs of ERI data are higher than those of MERRA-2 dataset and CWRF model in winter (0.96), spring (0.80) and summer (0.81), whereas MERRA-2 dataset has the highest TCC (0.76) in autumn. In winter and spring, ECP and NSAS schemes have good skills in simulating the interannual variations of P95 and considerable TCCs (0.79 and 0.81, respectively, in winter; 0.65 and 0.64, respectively, in spring) and RMSEs (1.37 and 1.63, respectively, in winter; 2.58 and 2.42, respectively, in spring). By contrast, ERI data produce a large RMSE (10.03) in summer, which is related to its systematic underestimation. Although KFeta and Tiedtke schemes better reproduce the interannual variation of the observed P95, there are serious overestimations, resulting in large RMSEs (16.20 and 15.46, respectively). The interannual variation of P95 simulated by ECP and NSAS schemes in autumn are similar, but ECP scheme underestimates extreme precipitation more seriously than NSAS scheme, resulting in relatively large RMSEs (4.96 and 3.22, respectively). BMJ scheme poorly simulates the interannual variation of P95 in all seasons in Central China and produces a large RMSE as a result of its systematic underestimation, especially in summer and autumn, with a TCC of roughly zero.

In South China (Fig. 8c, f, i, l and Fig. 9c), Tiedtke scheme gives the best simulation of the interannual variation of P95 in winter, with the highest TCC (0.91) and the smallest RMSE (2.52). In spring, the interannual variations of P95 simulated by ECP and KFeta schemes are equivalent (TCCs of 0.67 and 0.65, respectively) and are better than the other cumulus schemes. However, as a result of the influence of systematic underestimation, ECP scheme produces a larger RMSE (6.19) than KFeta scheme (5.05). In summer, MERRA-2 dataset gives the best reproduction of the interannual variation of the observed P95, with the highest TCC (0.7) and the lowest RMSE (3.72). The various cumulus schemes of CWRF model find it difficult to capture the interannual variation of P95 in summer, with serious overestimations or underestimations. In autumn, MERRA-2 dataset is more skillful than ERI data in simulating the interannual variation of P95 because ERI data gives a large underestimation and a false upward trend. Because the influence of assimilation on atmospheric feedback is limited by the measurements of precipitation, MERRA-2 dataset is more reliable than ERI data.

In general, the performance of all the cumulus parameterization schemes in CWRF model vary considerably over North, Central and South China. ECP scheme has the highest TCCs and lowest RMSEs in most seasons and regions, although NSAS scheme has slightly higher TCCs and smaller RMSEs in spring and summer in North China and in summer and autumn in Central China. BMJ scheme has the poorest performance, with a large underestimation. The simulation skills of KFeta and Tiedtke schemes are high in winter and spring in all three regions, but are low in summer and autumn. Overall, ECP scheme ranks as the best, NSAS scheme the second, and KFeta and Tiedtke schemes are third and fourth, respectively. BMJ scheme performs the poorest in reproducing the interannual variation of the observed P95. These results also confirm that the cumulus parameterization schemes play an important part in not only the spatial distribution of extreme precipitation, but also the regional mean characteristics of the interannual variation.

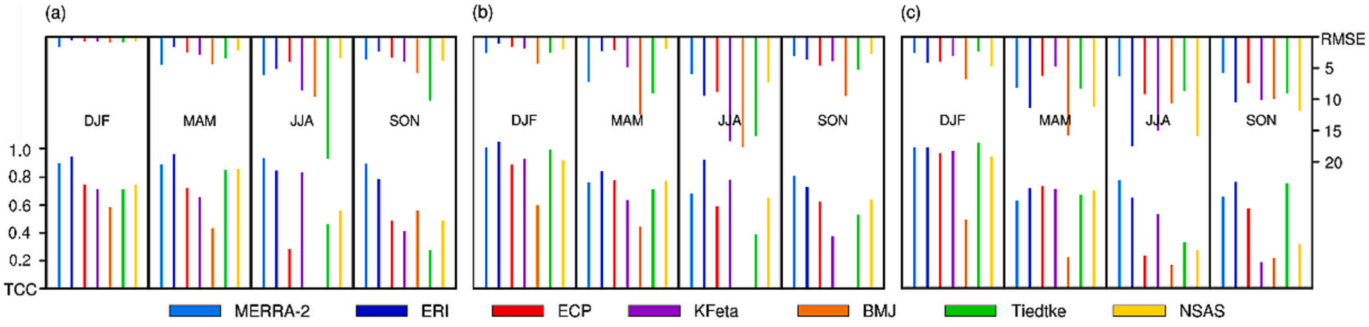

Fig. 9. TCC (scaled upward on the left) and root-mean-square error (RMSE; scaled downward on the right) of seasonally averaged P95 over (a) North China, (b) Central China and (c) South China in reanalysis data (ERI and MERRA-2) and simulation (CWRF model with ECP, KFeta, BMJ, Tiedtke, and NSAS cumulus parameterization schemes) for the time period 1980–2016.

3.4. Analysis of simulation biases in the extreme precipitation

Although it is not easy for climate models to reproduce the interannual variation of the observed P95, it is both crucial and challenging to trace the underlying physical processes for the success or failure of models to improve model skills in the future. We selected ECP scheme, which is good at simulating the interannual variation of P95 in China, and then analyzed the relationship between P95 biases and the key components of PL, PC, SWD, RSW, OLR, CRE, CWP and T2m.

We found the date of P95 event in every season of a particular year in each grid square and then calculated the biases of the simulated precipitation and their relevant variables from the corresponding observations on this date in each grid square. We first averaged these biases over North, Central and South China to obtain the time series of the interannual variations in every season and then calculated the TCCs between P95 biases and the relevant variable biases. The number of CWP, SWD, RSW, OLR and CRE observed samples are 30, 27, 27, 22 and 22 years, respectively, and the sample number of the remaining

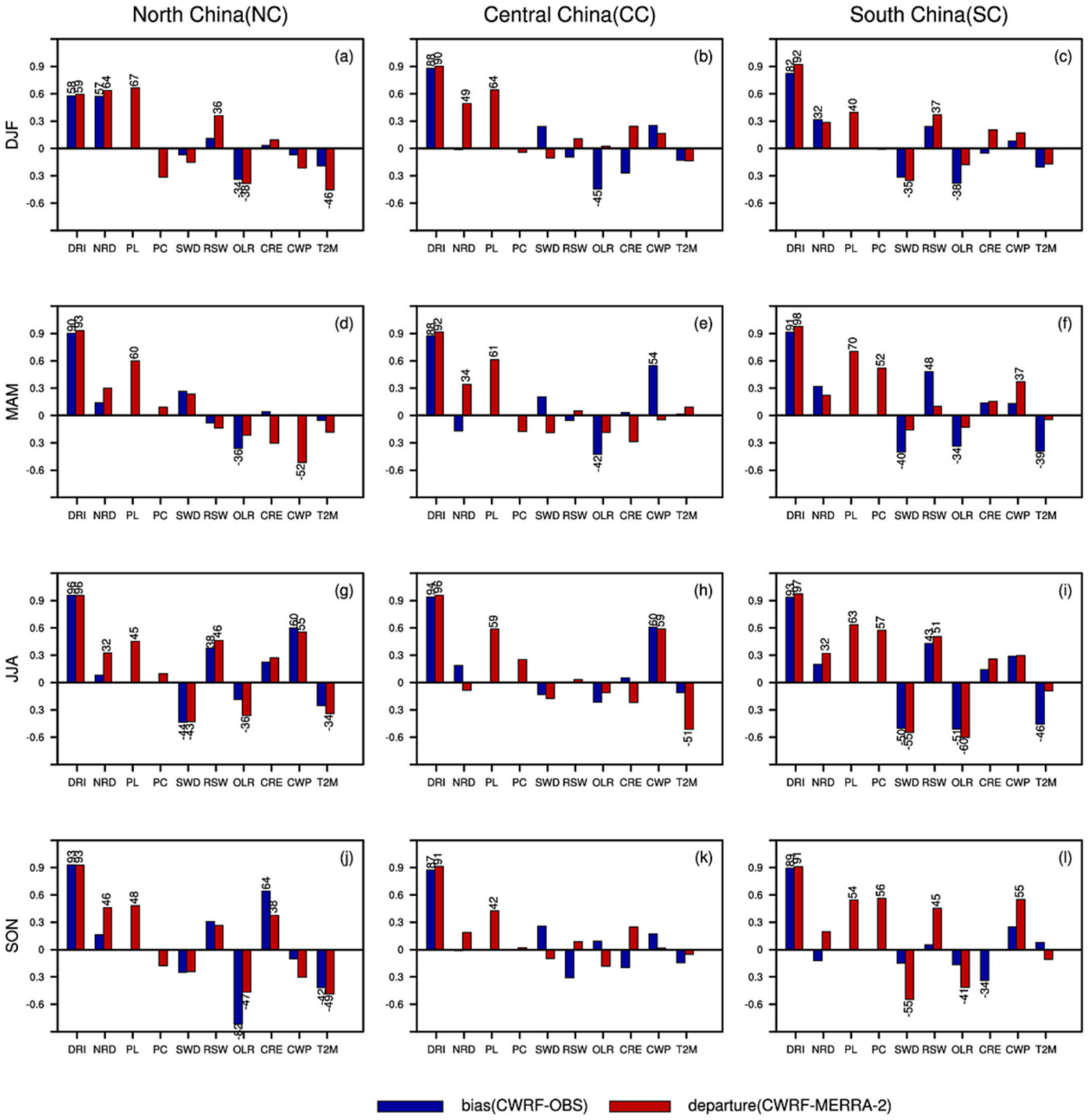

Fig. 10. Correlations of composite (CWRF using ECP scheme) P95 biases (blue) and departures (red) with fields that have observational data (DRI, NRD, SWD, RSW, OLR, CRE, CWP, and T2m) and P95 departures correlations with the rainfall components (PL and PC) in (a, d, g, j) North China, (b, e, h, k) Central China and (c, f, i, l) South China in (a–c) winter, (d–f) spring, (g–i) summer, and (j–l) autumn. If the significance reaches 95% confidence level, the bar is labeled with a number equal to the correlation coefficient times 100. (For interpretation of the references to colour in this figure legend, the reader is referred to the web version of this article.)

variables are all 37 years. In addition, the correlation relationships between P95 biases and the seasonal average values of DRI and NRD biases are also discussed.

Fig. 10 compares P95 biases and departures correlations with DRI, NRD, PL, PC, SWD, RSW, OLR, CRE, CWP and T2 m in four seasons. Because the date of P95 event in MERRA-2 dataset is different from that in observations, Fig. 10 compares the correlations based on the biases between the simulations and observations (blue column) and the departures between the simulations and MERRA-2 dataset (red column). The numbers marked on the figure indicate that the significance of the TCC passes the 95% confidence level.

In North China (Fig. 10a, d, g, j), there is a high correlation between P95 and DRI biases—that is, the TCC is the highest in summer (0.96), followed by autumn (0.93), spring (0.90) and winter (0.58). The TCCs between P95 and DRI departures of the simulation and MERRA-2 dataset also have a similar correlation (0.96 in summer, 0.93 in autumn, 0.93 in spring and 0.59 in winter). If the seasonal average precipitation intensity simulated by a model is strong (weak), then the P95 extreme precipitation produced by the model is also strong (weak). The TCC between P95 and NRD biases from the simulations and observations is only significant in winter (0.57). However, the TCCs between P95 and NRD departures from the simulation and MERRA-2 dataset significantly increase from spring to winter (0.30, 0.32, 0.46 and 0.64, respectively). Therefore, when a greater NRD are simulated, the model tends to overestimate P95, which is particularly obvious in North China. The TCCs between P95 and the PL departures is high and significant from spring to winter (0.60, 0.45, 0.48 and 0.67, respectively). By contrast, the TCCs between P95 and PC departures are not significant in all seasons. This means that P95 departures (from CWRF simulation and MERRA-2 dataset) in North China are less affected by the convective precipitation departures and more affected by the large-scale precipitation departures.

The TCC between P95 and the SWD biases is only significant and negative (−0.44) in summer. The TCC between P95 and the SWD departures from the simulation and MERRA-2 dataset also captures this feature (−0.43). The positive TCC between P95 and RSW biases is significant in summer (0.38), whereas the positive correlations of the departures are significant in both winter and summer (0.36 and 0.46, respectively). The P95 and OLR biases are significantly negatively correlated in winter, spring and autumn (−0.34, −0.36 and − 0.82, respectively). The P95 and OLR departures from the simulation and MERRA-2 dataset are only significantly negatively correlated in winter, summer and autumn (−0.38, −0.36 and − 0.47, respectively). The positive TCC between P95 and CRE biases is only significant in autumn (0.64) and the TCC (0.38) between P95 and CRE departures is weaker than the result of the simulations and observations. The correlation between P95 and CWP biases is only strong in summer (0.60). For the P95 and CWP departures, there is also a significantly positive correlation in summer (0.55). The negative TCC between P95 and T2 m biases is only significant in autumn (−0.42), whereas the correlations between P95 and T2 m departures are significant in winter, summer and autumn (−0.46, −0.34 and − 0.49, respectively). The TCCs between CWRF simulation and MERRA-2 dataset in North China reproduce well the sign and magnitude of the TCCs between the simulations and observations.

In Central China (Fig. 10b, e, h, k), there are high TCCs between P95 and DRI biases from spring to winter (0.88, 0.94, 0.87 and 0.88, respectively) and the correlations between P95 and DRI departures also show the same results (0.92, 0.96, 0.91 and 0.90, respectively). The TCCs between P95 and NRD biases are not significant in all seasons; they are almost zero in autumn and winter. However, the positive TCCs between P95 and NRD departures are significant in winter and spring (0.59 and 0.42, respectively). In addition, the TCCs between P95 and PL departures are high and significant from spring to winter (0.61, 0.59, 0.42 and 0.64, respectively). By contrast, the TCC between P95 and PC departures is not significant in any season. The negative TCCs between P95 and OLR biases are only significant in winter and spring (−0.45 and − 0.42, respectively), whereas different results are obtained for CWRF simulation and MERRA-2 reanalysis dataset. The TCCs between P95 and CWP biases are significant in spring and summer (0.54 and 0.60, respectively) and the correlation between P95 and CWP departures is only significant in summer (0.59). Furthermore, the TCCs across P95 with SWD, RSW, CRE and T2 m biases and departures are not significant in any season (except for −0.51 in autumn). Some of the biases and departures correlations even show the opposite signs in winter, spring and autumn. Considering the influence of satellite product estimations, the small number of available samples of observation data, the wide regional areas and complex climate systems, there are large uncertainties, which result in large differences between the correlations of biases and departures in Central China.

In South China (Fig. 10c, f, i, l), the correlations between P95 and DRI biases are still high from spring to winter (0.91, 0.93, 0.89 and 0.82, respectively). The correlations of the departures are also strong (0.98, 0.97, 0.91 and 0.92, respectively). The TCCs between P95 and PL departures in all seasons (0.70, 0.63, 0.54 and 0.40, respectively) are higher than those in North and Central China. The P95 and PC departures are significantly positively correlated in spring, summer and autumn (0.52, 0.57 and 0.56, respectively). There are negative TCCs between P95 and SWD biases in spring and summer (−0.40 and − 0.50, respectively), whereas the corresponding negative TCCs between and SWD departures strengthen significantly in summer and autumn (−0.55 and − 0.55, respectively). Positive TCCs between P95 and RSW biases occur in spring and summer (0.48 and 0.43, respectively), whereas the correlations between their departures are in summer and autumn (0.51 and 0.45, respectively). The correlations between the P95 and the OLR biases are negative in spring, summer and winter (−0.34, −0.51 and − 0.38, respectively), whereas the corresponding correlations of their departures are only significant in summer and autumn (−0.60 and − 0.41, respectively). The TCCs between the departures capture the TCCs between the biases from the simulations and observations in summer well. The results are fairly consistent, but are slightly different in spring and autumn. The TCCs between P95 and T2 m biases are only negative in spring and summer (−0.39 and − 0.46, respectively), but the correlations of the departures from the simulation and MERRA-2 dataset are not significant in any season.

We have shown that the correlations between the departures from the simulation and MERRA-2 dataset can reproduce the correlations between the biases of the key variables (DRI, NRD, PL, PC, SWD, RSW, OLR, CRE, CWP and T2m), especially in summer. The P95 departures are less affected by the convective precipitation departures, but are more affected by the large-scale precipitation (PL) departures in different regions. The relative contribution of convective precipitation (PC) to extreme precipitation may not be important, which also shows that there are other physical processes that have an important role in extreme precipitation events.

To understand the physical processes that affect P95 biases more comprehensively, we first established the consistency of P95 biases and departure correlations with the fields they resembled most closely. We then analyzed the correlations between the departures based on all the fields (SH, NSE, ET, MC, TPW, Q2m, W700, V850, FCL, FCH, RCT, CAPE, CIN, PBLH, LCL and LFC) from the simulation and MERRA-2 dataset. As a result of the lack of daily observational data for the atmospheric circulation, we use the 37-year samples from MERRA-2 dataset for this discussion.

Fig. 11 compares the seasonal correlation coefficients between P95 and all relevant field departures in North China. In winter (Fig. 11a, upper left triangle), the P95 departures have significant positive correlations with the CWP, RSW and W700 departures of 0.42, 0.32 and 0.42, respectively, and are negatively correlated with the OLR (−0.37) and TPW (−0.34) departures. In spring (Fig. 11a, lower right triangle), there are only significant positive correlations across P95 with ET (0.39) and W700 (0.37) departures. In summer (Fig. 11b, upper left triangle), there are positive correlations between P95 and MC (0.66), W700 (0.48), RSW

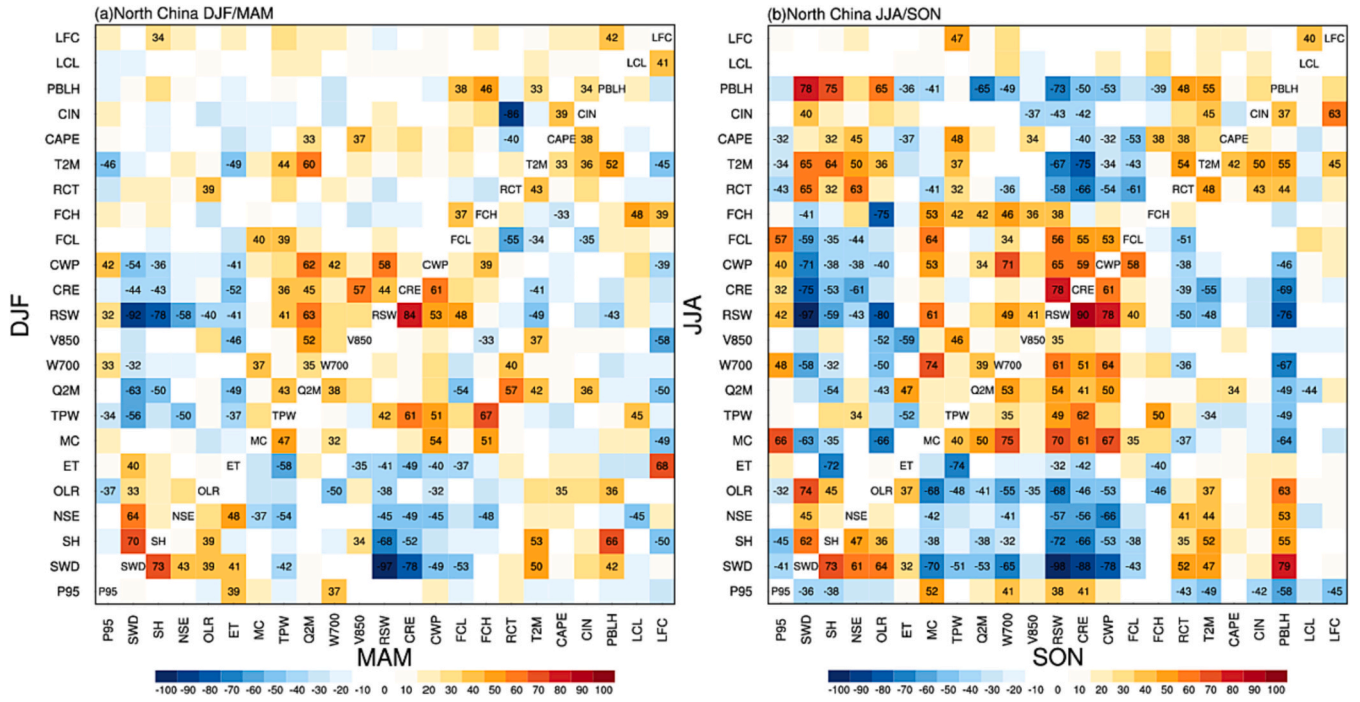

Fig. 11. Correlation coefficients between P95 and relevant variable departures (CWRF using ECP scheme) in North China in (a) winter (upper-left triangle) and spring (lower-right triangle) and in (b) summer (upper-left triangle) and autumn (lower-right triangle). The abscissa, ordinate and diagonal indicate P95 and each relevant variable. The correlation coefficient is multiplied by 100 and shown as shading. If the significance reaches 95% confidence level, the integer is marked on the corresponding box.

(0.42), CRE (0.32), CWP (0.40) and FCL (0.57) departures and negative correlations between P95 and SWD (−0.41), SH (−0.45), OLR (−0.32), RCT (−0.43), T2 m (−0.34) and CAPE (−0.32) departures. In autumn (Fig. 11b, lower right triangle), the P95 and MC (0.52), W700 (0.41), RSW (0.38) and CRE (0.41) departures are significantly positive correlated, whereas P95 and SWD (−0.36), SH (−0.38), RCT (−0.43), T2 m (−0.49), CIN (−0.42), PBLH (−0.58) and LFC (−0.45) departures are significantly negative correlated. W700 is the common significant positive correlation factor for P95 departures in all seasons and RSW is the common significant correlation factor in summer, autumn and winter.

In Central China, positive correlations are found between P95 and ET (0.34), MC (0.42), W700 (0.59), CWP (0.36) and FCL (0.49) departures in winter (Fig. 12a, upper triangle left). The P95 departures are significantly negative correlated with the SH (−0.47) and TPW (−0.41)

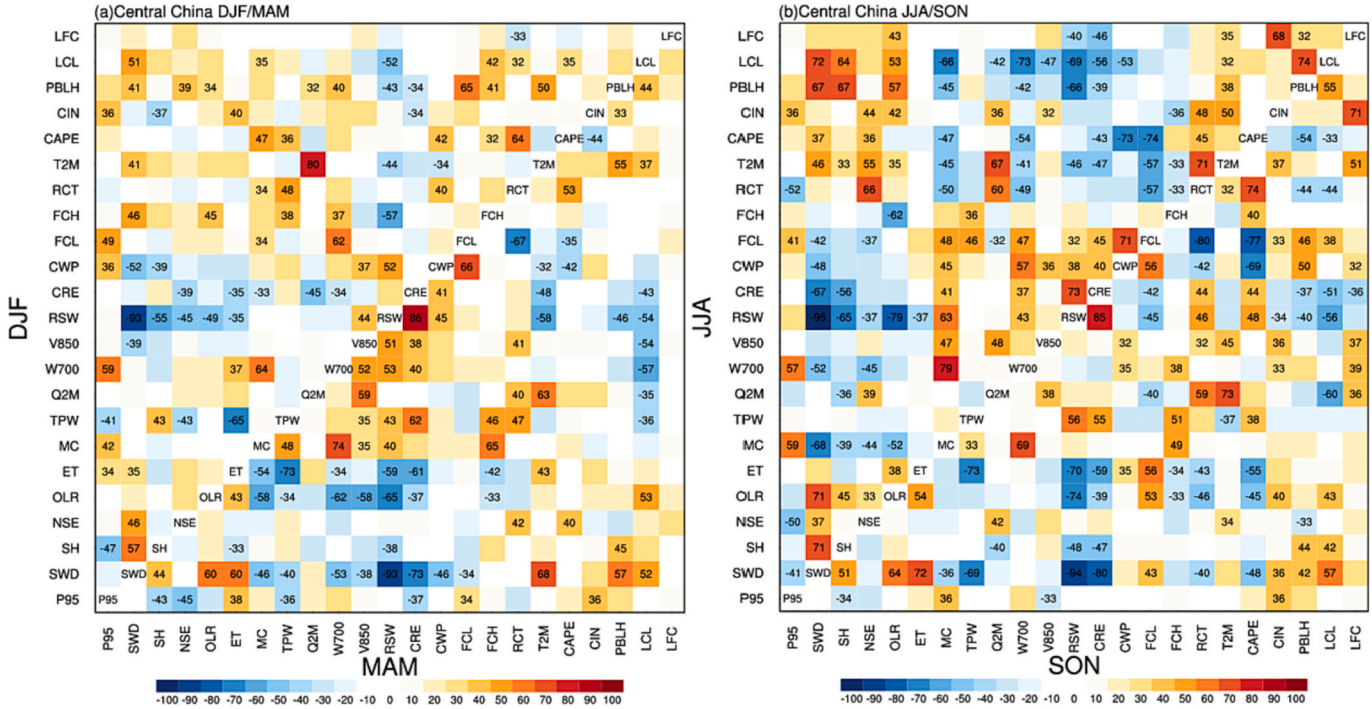

Fig. 12. Same as Fig. 11, but for Central China.

departures. In spring (Fig. 12a, lower triangle right), the P95 departures have significant positive correlations with the ET (0.38), FCL (0.34) and CIN (0.36) departures and negative correlations with the SH (−0.43), NSE (−0.45), TPW (−0.36) and CRE (−0.37) departures. In summer (Fig. 12b, upper triangle left), the P95 departures are significantly positively correlated with MC (0.59), W700 (0.57), FCL (0.41) and CIN (0.36) departures and significantly negatively correlated with SWD (−0.41), NSE (−0.50) and RCT (−0.52) departures. In autumn (Fig. 12b, lower triangle right), positive correlations are found between P95 and MC (0.36) and CIN (0.36) departures and negative correlations between P95 and SH (−0.49) and V850 (−0.33) departures. The SH is the common significant negative correlation factor for P95 departures in autumn, winter and spring. The MC is the common significant positive correlation factor for P95 departures in summer, autumn and winter. The CIN in spring, summer and FCL in winter, spring and summer are common high correlation factors.

In South China, the P95 departures are positively correlated with MC (0.43), V850 (0.43) and RSW (0.36) in winter (Fig. 13a, upper triangle left), whereas they are significantly negatively correlated with the SWD (−0.37) and SH (−0.42). In spring (Fig. 13a, lower triangle right), the P95 departures have significant positive correlations with MC (0.83), W700 (0.83), CAPE (0.42), LCL (0.33) and LFC (0.42) departures and negative correlations with the Q2 m (−0.35), V850 (−0.45) and RCT (−0.57) departures. In summer (Fig. 13b, upper triangle left), there are positive correlations of P95 departures with MC (0.62), TPW (0.32), Q2 m (0.32), W700 (0.58), RSW (0.43) and CWP (0.41) departures, but negative correlations of P95 departures with SWD (−0.48), SH (−0.42), NSE (−0.50), OLR (−0.53), ET (−0.42) and RCT (−0.33) departures. In autumn (Fig. 13b, lower triangle right), the P95 departures are positively correlated with MC (0.75), W700 (0.59), RSW (0.44) and FCL (0.48) departures, but negatively correlated with the SWD (−0.53), SH (−0.49) and OLR (−0.47) departures. The MC is the common significant positive correlation factor for P95 departures in all seasons, whereas W700 is the common significant positive correlation factor in spring, summer and autumn. RSW, SWD and SH have common effects on P95 departures in summer, autumn and winter.

From these analyses, it can be seen that the SH significantly affects P95 departures and the SWD provides an energy source for the sensible heat. The NSE represents the net radiation flux minus the surface heat (the latent heat plus the sensible heat) flux, which also includes the SWD and SH effects. Figs. 11–13 also reflect the high correlations among them. The ET is an important part of the water cycle. An insufficient (excessive) supply of water vapor could directly result in the underestimation (overestimation) of P95 in different regions. Their impacts on extreme precipitation strongly depend on the region and season. The ET and MC ensure a sufficient supply of water vapor, mainly measured by the TPW. There are also close relationships among the OLR, RSW and CRE. Deeper cumulus clouds produce less OLR, so the deeper the optical depth of the cloud, the more the RSW, resulting in a strong CRE, which cools the Earth's atmospheric system. An underestimation of deep convection may reduce the simulated amount of extreme precipitation.

Compared with PC, the ratio of convective precipitation to total precipitation (RCT), as an alternative to precipitation efficiency, has more complex impacts on the simulation P95 and its role is uneven in different regions and seasons. A large SWD can cause a warm T2m, much SH, a wet Q2 m and a high PBLH in spring and summer. In addition, a warm T2 m affects the reduction in FCL and FCH, thus affecting the changes in the OLR, RSW and CRE. However, the correlations among these variables weaken in magnitude in autumn and winter. With seasonal changes, the regional precipitation process system changes and the role of the surface–atmosphere–cloud–radiation interactions change significantly. Other relevant variables in North, Central and South China are also strongly related, especially the PBLH in summer. The larger SWD and sensible heat lead to a higher PBLH, a higher cumulus base (less FCL) and a smaller cloud depth (less FCH). Figs. 11–13 also show more complex relationships among all fields, which require more advanced machine learning technologies and methods to clarify and to determine the most reasonable mechanism behind P95 simulation departures.

3.5. *Underlying physical processes of extreme precipitation simulation biases*

Extreme precipitation is caused by complex changes in the climate system in different regions. Based on our analysis, it is clear that there is a strong correlation among all fields. We first fitted all the possible

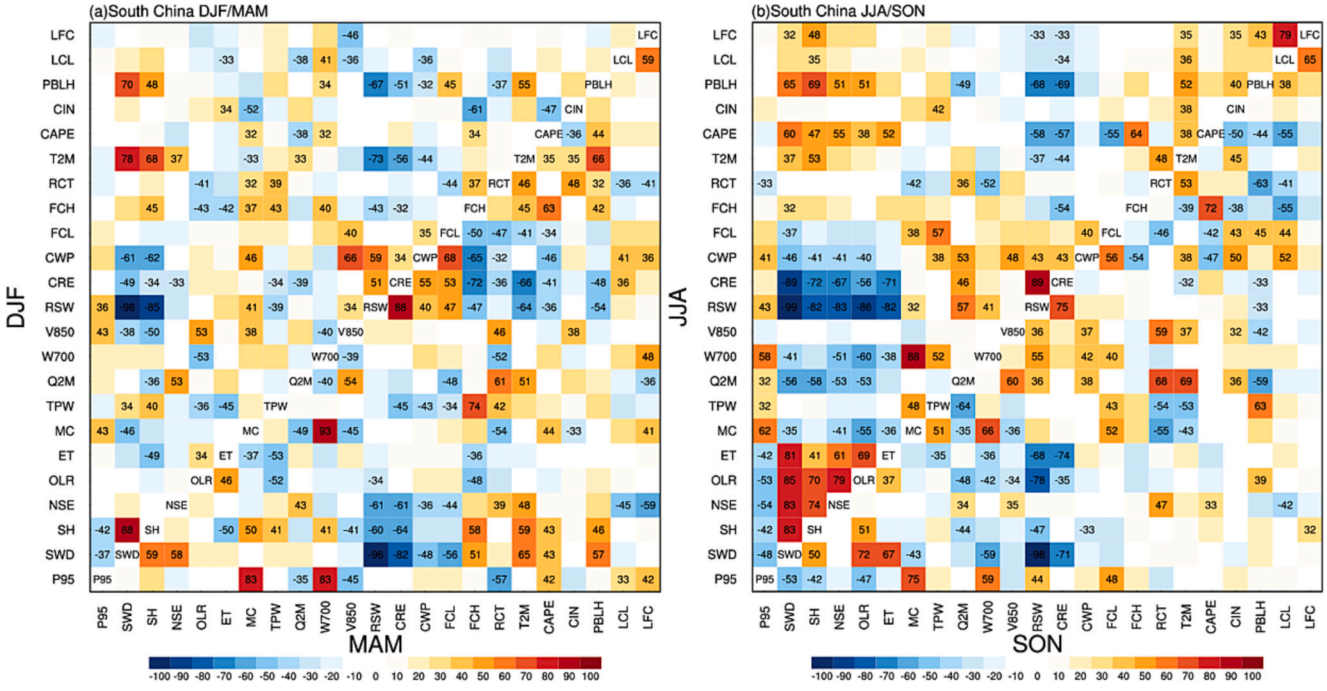

Fig. 13. Same as Fig. 11, but for South China.

combinations of the 22 preselected variables and then selected the regression model based on the following three principles: it only contains significant variable factors; the total explained variance (R^2) is the largest, and the Akaike information criterion is the smallest. Akaike information criterion (AIC) was proposed by Akaike (1974) to measure the goodness of fit of a statistical model. It is grounded in the concept of entropy, offering a relative measure of the lost information when a given model is used to describe reality and can be weighed against the precision and complexity of the model. In general, the smaller the AIC value, the better the model performance. According to the recommendation of Burnham and Anderson (2004), other competition models are not considered since the AIC differences of our selected models from the minimum reference are >10. In this way, all possible models are tested and an optimum set of variables is screened out.

Table 3 shows the main factors and performance indicators relevant to P95 departures in the regression models established for North, Central and South China. By comparing the relative importance of each factor in different regression models, we find that the first and second factors that contribute the most to the selected model are the same, so the underlying impact on P95 departures can be discussed simply. Table 3 shows that most of the regression models can explain changes in P95 departures of >74% (total explained variance $R^2 > 74\%$), except for North China in winter, Central China in autumn and South China in winter. The simulation results are explained according to the relative importance (RI) of the first and second factors.

In North China, the PBLH and RSW departures are the first and second most important factors affecting P95 departures in winter. They can explain 52.38% of the influence on P95 departures. A lower PBLH and greater RSW lead to larger P95 departures. In spring, more water from surface evapotranspiration (RI = 18.72%) and a stronger W700 (RI = 16.03%) have leading roles in P95 departures. In summer, the P95 departure is dominated by the positive direct effect of the MC departure, the relative importance of which reaches 32.24%, where a stronger MC produces more extreme precipitation. The SH is the second important factor affecting P95 departure (RI = 23.01%). The more extreme the precipitation, the more heat it consumes. In autumn, the LCL (RI = 26.87%) and PBLH (RI = 17.55%) departures are the first and second most important factors, respectively, determining P95 departures. The combination of a lower LCL and PBLH results in large P95 departures, with a total relative importance of 44.42%.

In Central China, the W700 (RI = 25.66%) and TPW (RI = 20.47%) departures are the first and second most important factors, respectively, determining P95 departures. Strong ascending movement and a low TPW lead to large amounts of extreme precipitation in winter. In spring, the P95 departures are determined by two energy effects: the SH (RI = 30.26%) and the NSE (RI = 21.63%) departures. The total relative importance of the two factors reaches 51.89%. A large amount of sensible heat is released into the atmosphere and combines with the surplus NSE for the consumption of precipitation, which results in a reduction in P95 departures. By contrast, the P95 departure are mainly affected by two opposite factors: a positive MC (RI = 27.12%) and a negative CAPE (RI = 17.64%) departures in summer. Strong MC and low CAPE departures lead to large P95 departures. In autumn, the regression model only can explain 66% (total explained variance) of the changes in P95 departures. The PBLH (RI = 18.39%) and CWP (RI = 14.70%) departures are the first and second important factors, respectively, determining P95 departures.

In South China, the regression models in spring, summer and autumn can explain >80% of the changes in P95 departures, but the model in winter has a poor interpretation effect with a total explained variance of only 63% due to the influence of other independent variables and systematic and random errors. In winter, strong V850 (RI = 26.72%) and MC (RI = 19.37%) departures lead to large P95 departures and the total relative importance reaches 46.09%. In spring, the P95 departures are dominated by a positive effect of the W700 (RI = 36.28%) and MC (RI = 31.52%) departures. The relative importance of the two factors reaches a total of 67.80%. A continuous supply of water vapor supply leads to large amounts of extreme precipitation. In summer, the SWD (RI = 22.10%) and RSW (RI = 19.14%) have negative impacts on P95 departures, whereas a weaker energy supply and less reflected shortwave radiation at the top of atmosphere result in larger amounts of extreme precipitation. In autumn, the P95 departures are determined by two opposite direct effects: positive MC (RI = 37.11%) and negative SWD (RI = 22.96%) departures. A strong moisture convergence departure causes a large P95 departure and a large supply of surface energy decreases some of the impact on P95 departures.

The selection of the cumulus parameterization scheme therefore affects the relative importance of each factor in P95 biases and has an important role through the interactions among various factors in different regions and seasons. This determines the simulation ability of CWRF model for extreme precipitation in China.

Table 3
Main factors and indicators relevant to P95 departures in North, Central and South China. The symbol "−" indicates the factor has a negative role.

Domain	Season	Main factors and signs	Total explained variance (R^2)	Akaike information criterion	First and second factors (relative importance)	
North China	DJF	SWD, SH, NSE, RSW, FCH, −T2M, −PBLH, LCL	0.67	83.1	PBLH (28.61%)	RSW (23.77%)
	MAM	−NSE, OLR, ET, W700, −CRE, CWP, −FCH, RCT, −T2M, −CAPE	0.78	74.3	ET (18.72%)	W700 (16.03%)
	JJA	SWD, −SH, MC, −Q2M, V850, −RCT, CIN	0.74	74.3	MC (32.24%)	SH (23.01%)
	SON	SWD, −TPW, Q2M, CRE, CWP, FCH, −T2M, −CAPE, −PBLH, −LCL	0.80	68.5	LCL (26.87%)	PBLH (17.55%)
Central China	DJF	SWD, −NSE, OLR, MC, −TPW, W700, CRE, CWP, −RCT, −T2M	0.75	76.3	W700 (25.66%)	TPW (20.47%)
	MAM	−SH, −NSE, −ET, MC, −TPW, −RSW, −LFC	0.76	70.5	SH (30.26%)	NSE (21.63%)
	JJA	−ET, MC, −V850, −CRE, −T2M, −CAPE, −PBLH, LCL	0.84	57.0	MC (27.12%)	CAPE (17.64%)
	SON	OLR, ET, Q2M, RSW, −CRE, −CWP, −FCL, −T2M, −CAPE, PBLH	0.66	88.5	PBLH (18.39%)	CWP (14.70%)
South China	DJF	−OLR, MC, W700, V850, −FCL, −RCT, −CAPE, −LFC	0.63	87.1	V850 (26.72%)	MC (19.37%)
	MAM	−SH, ET, MC, Q2M, W700, −V850, −RCT, PBLH, LCL	0.88	44.7	W700 (36.28%)	MC (31.52%)
	JJA	−SWD, −V850, −RSW, −CRE, CWP, −FCL, −RCT, PBLH	0.83	57.5	SWD (22.10%)	RSW (19.14%)
	SON	−SWD, MC, −V850, −CRE, −FCL, FCH, IN, −LFC	0.84	57.1	MC (37.11%)	SWD (22.96%)

4. Conclusion and discussion

We used CWRF model to analyze simulations of extreme precipitation in China from 1980 to 2016 and focused on the sensitivity and dependence of extreme precipitation events on different cumulus parameterization schemes in the three key regions of North, Central and South China. By comparing ERI data and five cumulus parameterization schemes in CWRF model in simulations of extreme precipitation events, we selected ECP scheme, which has a relatively good simulation effect, to investigate the underlying physical processes explaining how the cumulus parameterization scheme determines the ability of CWRF model to simulate extreme precipitation events in China.

(1) The CWRF model using the ECP scheme performs better than the ERI on spatial distribution and temporal variation of seasonally averaged general precipitation and extreme precipitation. Although there are 5–10 mm/day extreme precipitation biases of interannual variation in the CWRF, it can better represent the location and intensity of two rain bands in the Yangtze River basin and across South China, and it has <2 mm/day and 5–10 day biases of the observed interannual variation of seasonally averaged precipitation and NRD, respectively. In particular, the CWRF is more consistent with the monthly variation of precipitation, NRD and P95 over China, which the ERI systematically overestimates. This gives better results than ERI data, showing a large improvement with added value in mountainous and coastal areas. The different cumulus parameterization schemes vary substantially in their model biases and skill scores in different regions and seasons. The P95 biases of ECP scheme are lowest in North China and this scheme gives the best performance with the highest ETS score in summer. KFeta scheme captures the spatial pattern of P95 and produces a higher PCC and smaller standard deviation than ECP scheme, and with an ETS followed ECP scheme. In Central China, the spatial distribution of P95 simulated by CWRF model with ECP and NSAS schemes in all seasons are the most realistic. ECP scheme gives an excellent performance in the simulation, with the highest PCC and ETS (except in autumn) among the five cumulus schemes. KFeta and Tiedtke schemes substantially overestimate P95 in all seasons, whereas BMJ scheme substantially underestimates P95 and lacks simulation skills. ECP scheme perfectly reproduces the heavy rain band in coastal areas of South China, especially in summer. However, ECP scheme has the highest ETS in this region, although it significantly underestimates the extreme precipitation. Although KFeta and Tiedtke schemes overestimate the magnitude of P95, they have high ETS values in winter and spring. Some cumulus schemes capture extreme precipitation under forcing by mixed weather systems and convective systems. For example, although KFeta scheme cannot capture the spatial pattern very well, its simulations of P95 in South China in spring and autumn are good. NSAS scheme overestimates a large range of NRDs in Central China in spring and autumn, but its simulation of P95 is better than that using ECP scheme. ECP scheme can be cooperated with other physical parameterization schemes (e.g., radiation, microphysics and aerosol optical depth) to further improve the simulation skills of CWRF model.

(2) The choice of cumulus parameterization scheme has a significant impact on the simulation of extreme precipitation, not only the climatological average spatial distributions, but also the regionally averaged interannual variation. The ERI reanalysis data substantially underestimates the interannual variation of P95, whereas ECP scheme gives quite good simulation of the interannual variation of P95 in most seasons over North, Central and South China (the highest TCC and smallest RMSE). NSAS scheme ranks second, followed by KFeta, Tiedtke and BMJ schemes. For the ECP scheme, we computed the correlation coefficients of the departures between P95 and relevant variables (including DRI, NRD, SWD, SH, NSE, OLR, ET, MC, TPW, Q2m, W700, V850, RSW, CRE, CWP, FCL, FCH, RCT, T2m, CAPE, CIN, PBLH, LCL and LFC). Our results show that, except for a low correlation in Central China, the correlations of the differences between the simulations and MERRA-2 dataset reproduce well the magnitudes and signs of the bias correlations between the simulations and observations in most seasons over both North and South China. The MERRA-2 dataset is therefore a good choice for use as reference data in the absence of observational circulation data. We also found significant correlations between P95 departures and the departures of the 22 relevant variables. The correlation coefficients varied from −0.96 to 0.90 in different regions and seasons and some variables were interdependent, which promoted or offset the formation of extreme precipitation.

(3) Based on the complex relationships between P95 departures and the 22 relevant variable departures in the simulation using the ECP scheme, we selected the optimum model using the all-subsets regression method to quantify their relative importance to P95 departures and tried to determine the first and second factors contributing the most to P95 departures. In North China, the P95 departures are mainly affected by the PBLH and RSW departures in winter (total RI = 52.38%), the ET and W700 departures in spring (total RI = 34.75%), the MC and SH departures in summer (total RI = 55.25%), and the LCL and PBLH departures in autumn (total RI = 44.42%). In Central China, the P95 departures are dominated by the W700 and TPW departures in winter (total RI = 46.13%), the SH and NSE departures in spring (total RI = 34.75%), the MC and CAPE departures in summer (total RI = 44.76%), and the PBLH and CWP departures in autumn (total RI = 33.09%). In South China, the P95 departures are influenced by the V850 and MC departures in winter (total RI = 46.09%), the W700 and MC departures in spring (total RI = 67.80%), the SWD and RSW departures in summer (total RI = 41.24%), and the MC and SWD departures in autumn (total RI = 60.07%). Of the 12 regression models, the listed relative importance of the first and second factors (occurring times) are MC (5), PBLH (3), W700 (3), SH (2), RSW (2), ET (1), LCL (1), TPW (1), SWD (1), NSE (1), V850 (1), CAPE (1) and CWP (1). Their relative importance and relevance to P95 largely depend on the regions and seasons.

We investigated the influence of different cumulus parameterization schemes in CWRF model on the simulations of extreme precipitation over China. Our analyses showed that there are many differences and similarities of precipitation simulations between the US and China when using the five cumulus parameterization schemes. Compared with the results of Sun and Liang (2020a, 2020b), we found that the control experiment of the CWRF model corresponds to the ECP scheme run, which better represents the seasonal average P95 in the US than in China. And the ECP scheme reproduces the extreme precipitation events and their peaks near the coastline in the US and China due to its various weights and different closure options between land and ocean, but precipitation is overestimated in both China and the US. Except for a long and narrow rain band along the coastline, the ECP scheme underestimates P95 of a large range in eastern China. The KFeta scheme produces reasonable P95 and relatively small biases in the US, while it substantially overestimates P95 between the Yangtze River and Pearl River basins. The Tiedtke scheme has opposite simulation biases of P95 in the US and China. And the Tiedtke scheme performances abnormally, which yields substantially large spatial variability both in the US and China. The ability of the NSAS scheme to capture extreme precipitation in China is higher than that in the US.

For interannual variation of seasonal P95, the ECP scheme slightly underestimates P95 magnitude and variability in China, compared to its overestimates in the US. The ECP scheme best simulates P95 interannual variation among all the schemes, both in the US and China, with the

highest TCC and smallest RMSE. The departures of the Tiedtke scheme from the interannual variation of P95 in the US are not as large as those in China. Except for South China, the NSAS scheme is equivalent to the ECP scheme in China but worse in the US, which has a notably lower correlation and larger RMSE. The BMJ scheme fails totally to simulate the extreme precipitation characteristics both in the US and China. Except for the impacts of different monsoon systems in the US and China, the sensibility of different cumulus schemes to P95 under mixed synoptic and topography forcing may lead to large differences in simulating extreme precipitation. In addition, we noticed that the CWRF still has a significantly enhanced ability to capture extreme precipitation after combining the ECP cumulus scheme with other physical schemes. Therefore, through the comparison of different cumulus schemes used in the US and China, we obtain some preliminary conclusions that provide a reference for selecting cumulus parameterization schemes in regional climate models. The version used in this study does not represent the best performance of the CWRF in China; and we can examine an ensemble of physics configurations to further improve the skill of the CWRF in China.

As stated above , different regions and seasons have different responses to the simulation of extreme precipitation events with different cumulus parameterization schemes. Future regional climate simulations should focus more on the development of more realistic physical processes. The choice of cumulus parameterization scheme affects the relative importance of various factors to the simulation of P95 and produces a marked effect through the interactions among them, further influencing the performance of CWRF model in simulating extreme precipitation in China.

In this study, the model resolution is 30 km. Cumulus parametrization schemes are often designed to describe indiscernibility process due to grid size when the size is >10 km. With the improvement of resolution, the model can explicitly express some convective processes when the grid is smaller than 4 km or close to the diameter of the convective system, and the cumulus parameterization process is closed (Arakawa and Jung, 2011). However, there is a “gray zone” of cumulus convection parameterization scheme when the resolution is between 4 and 10 km. The closure assumptions of cumulus convection parameterization are no longer applicable; and the model can only partially express the convection process (Hong and Dudhia, 2012). The performance of cumulus convective parameterization scheme under different resolution and its application in the “gray zone” need to be further studied in the future.

The regression models established in this study are relatively simple and only roughly discuss the influence of various factors on P95 simulation departures. In fact, the 22 factors selected by referring to the research of Sun and Liang (2020b) are not independent and there are strong correlations among them (Figs. 11–13). However, using these highly correlated factors as predictors to establish regression models would lead to multicollinearity. The regression model might be unstable because of the repeated calculation of specific factors or overfitting. Sun and Liang (2020b) designed a structural equation regression model, which not only solved the problem of multicollinearity, but also reduced the dimensions by constructing four potential factors so that the causal relationship behind the simulation departures could be better explained. Hundreds of millions of alternative combinations of the structural equation regression models for P95 simulation departures can be successfully established in different regions and seasons. However, this requires not only machine learning by supercomputers, but also supercomputers with a huge storage capacity to optimize the filter and to determine the unique and optimum structural equation regression model for each region and season within certain constraints.

We compare the sensitivity of different cumulus parameterization schemes to extreme precipitation, and identify which schemes can best capture extreme precipitation processes in Figs. 4–9. P95 results from the complex climate system as a whole and its model bias mechanisms are extremely challenging to understand. Sun and Liang (2020b) recognized this challenge, and used structural equation regression model for supercomputing diagnosis. The underlying physical processes will definitely depend on the system coupling of all physics parameterizations and dynamics’ representations. As such, this study focuses on a single cumulus parameterization, choosing the high performer ECP scheme as the first priority to explore the underlying physical processes. Exploring other cumulus schemes will take more time and should be done in the future.

CRediT authorship contribution statement

Shiyu Zhang: Conceptualization, Methodology, Software, Validation, Formal analysis, Writing – original draft, Writing – review & editing. **Minghao Wang:** Conceptualization, Methodology, Formal analysis, Writing – original draft, Writing – review & editing, Supervision, Project administration, Funding acquisition. **Lanning Wang:** Conceptualization, Methodology, Writing – review & editing, Supervision, Funding acquisition, Resources. **Xin-Zhong Liang:** Conceptualization, Methodology, Writing – review & editing, Supervision, Funding acquisition, Resources. **Chao Sun:** Investigation, Methodology, Writing – review & editing. **Qingquan Li:** Conceptualization, Methodology, Formal analysis, Writing – original draft, Writing – review & editing, Supervision, Project administration, Funding acquisition.

Declaration of Competing Interest

The authors declare that they have no known competing financial interests or personal relationships that could have appeared to influence the work reported in this paper.

Data availability

The authors do not have permission to share data.

Acknowledgements

We would thank three anonymous reviewers for providing valuable recommendations. This study was jointly supported by the National Key Research and Development Program of China (2022YFE0136000), the National Natural Science Foundation of China (U2242207), the Second Tibetan Plateau Scientific Expedition and Research Program of China (2019QZKK0208), the Strategic Priority Research Program of the Chinese Academy of Sciences (XDA20100304), the National Natural Science Foundation of China (41965005), the National Key Research and Development Program of China (2016YFA0602200). Sun and Liang were partially supported by the U.S. National Science Foundation Innovations at the Nexus of Food, Energy and Water Systems under Grant EAR1903249. We thank the Maryland Advanced Research Computing Center (USA) and the Wuxi National Supercomputing Center (China) for archiving CWRF source codes and conducting model simulations. We acknowledge China Meteorological Administration (CMA) for providing the gridded daily analysis surface data as the observational reference (CN05.1).

Appendix A. Supplementary data

Supplementary data to this article can be found online at https://doi.org/10.1016/j.atmosres.2023.106636.

References

Akaike, H., 1974. A new look at the statistical model identification. Autom. Control 19, 716–723.
Alexopoulos, E., 2010. Introduction to Multivariate Regression Analysis. Hippokratia 14, 23–28.
Allen, M.R., Ingram, W.J., 2002. Constraints on future changes in climate and the hydrologic cycle. Nature. 419, 224–232.

Arakawa, A., Jung, J.H., 2011. Multiscale modeling of the moist-convective atmosphere: a review. Atmos. Res. 102, 263–285.
Bechtold, P., Kohler, M., Jung, T., Doblas-Reyes, F., Leutbecher, M., Rodwell, M.J., Vitart, F., Balsamo, G., 2008. Advances in simulating atmospheric variability with the ECMWF model: from synoptic to decadal timescales. Q. J. R. Meteorol. Soc. 134, 1337–1351.
Betts, A.K., Miller, M.J., 1986. A new convective adjustment scheme. Part II: single column tests using GATE wave, BOMEX, and arctic air-mass data sets. Q. J. R. Meteorol. Soc. 112, 693–709.
Burnham, K.P., Anderson, D.R., 2004. Multimodel inference: understanding AIC and BIC in model selection. Sociol. Methods Res. 33, 261–304.
Chen, S., Gan, T.Y., Tan, X., Shao, D., Zhu, J., 2019. Assessment of CFSR, ERA-Interim, JRA-55, MERRA-2, NCEP-2 reanalysis data for drought analysis over China. Clim. Dyn. 53, 737–757.
Collow, A.B.M., Bosilovich, M.G., Koster, R.D., 2016. Large-scale influences on summertime extreme precipitation in the northeastern United States. J. Hydrometeorol. 17, 3045–3061.
Coumou, D., Rahmstorf, S., 2012. A decade of weather extremes. Nat. Clim. Chang. 2, 491–496.
Coy, L., Wargan, K., Molod, A.M., McCarty, W.R., Pawson, S., 2016. Structure and dynamics of the quasi-biennial oscillation in MERRA-2. J. Clim. 29, 5339–5354.
Dai, A., 2006. Precipitation characteristics in eighteen coupled climate models. J. Clim. 19, 4605–4630.
Dee, D.P., Uppala, S.M., Simmons, A.J., Berrisford, P., Poli, P., Kobayashi, S., Andrae, U., Balmaseda, M.A., Balsamo, G., Bauer, D.P., Bechtold, P., 2011. The ERA-interim reanalysis: configuration and performance of the data assimilation system. Q. J. R. Meteorol. Soc. 137, 553–597.
Doswell, C.A., Brooks, H.E., Maddox, R.A., 1996. Flash flood forecasting: an ingredients-based methodology. Weather Forecast. 11, 560–581.
Fan, J., Hu, T.C., Truong, Y.K., 1994. Robust non-parametric function estimation. Scand. J. Stat. 21, 433–446.
Gan, S.H., Liu, S.Y., Yan, Y., Mao, W.P., 2015. A trial study of inverse distance weighting interpolation (IDW) in precipitation forecast test. In: Annual Meeting of the Chinese Meteorological Society S3 Military Numerical Weather Forecast Technology and Application, pp. 34–39.
Gandin, L.S., Murphy, A.H., 1992. Equitable skill scores for categorical forecasts. Mon. Weather Rev. 120, 361–370.
Gao, X.J., Shi, Y., Han, Z.Y., Wang, M.L., Wu, J., Zhang, D.F., Xu, Y., Giorgi, F., 2017. Performance of RegCM4 over major river basins in China. Adv. Atmos. Sci. 34, 441–455.
Grell, G.A., Dévényi, D., 2002. A generalized approach to parameterizing convection combining ensemble and data assimilation techniques. Geophys. Res. Lett. 29, 381–384.
Han, J., Pan, H.L., 2011. Revision of convection and vertical diffusion schemes in the NCEP global forecast system. Weather Forecast. 26, 520–533.
Hong, S.Y., Dudhia, J., 2012. Next-generation numerical weather prediction: Bridging parameterization, explicit clouds, and large eddies. Bull. Am. Meteorol. Soc. 93, ES6-ES9.
Huang, A.N., Zhang, Y.C., Zhu, J., 2008. Impacts of physical process parameterizations on simulation of the diurnal variations of summer precipitation over China. Adv. Earth. Sci. (in Chinese). 23, 1174–1184.
IPCC, 2021. Climate Change 2021: The Physical Science Basis [M/OL]. Cambridge University Press. https://www.ipcc.ch/report/ar6/wgl/downloads/ (report/ IPCC_AR6_WGI_Full_Report.pdf).
Janjic, Z.I., 1994. The step-mountain eta coordinate model: further developments of the convection, viscous sublayer and turbulence closure schemes. Mon. Weather Rev. 122, 927–945.
Kain, J.S., 2004. The Kain-Fritsch convective parameterization: an update. J. Appl. Meteorol. 43, 170–181.
Kain, J.S., Fritsch, J.M., 1993. Convective parameterization for mesoscale models: the Kain–Fritcsh scheme. Meteorol. Monogr. 24, 165–170.
Kang, I.S., Yang, Y.M., Tao, W.K., 2015. GCMs with implicit and explicit representation of cloud microphysics for simulation of extreme precipitation frequency. Clim. Dyn. 45, 325–335.
Karlsson, K.G., Anttila, K., Trentmann, J., Stengel, M., Meirink, J.F., Devasthale, A., Hanschmann, T., Kothe, S., Jääskeläinen, E., Sedlar, J., Benas, N., van Zadelhoff, G. J., Schlundt, C., Stein, D., Finkensieper, S., Håkansson, N., Hollmann, R., Fuchs, P., Werscheck, M., 2017. CLARA-A2: CM SAF cloud, albedo and surface radiation dataset from AVHRR data–Edition 2. Satellite application facility on climate monitoring. https://doi.org/10.5676/EUM_SAF_CM/CLARA_AVHRR/V002.
Li, Q.X., 2011. Introduction to the Study of Climate Data Homogeneity. China Meteorological Press.
Li, H., Feng, L., Zhou, T., 2010. Multi-model projection of July–August climate extreme changes over China under CO2 doubling. Part I: Precipitation. Acta Meteor. Sin. 28, 433–477.
Li, F., Rosa, D., Collins, W.D., Wehner, M.F., 2012. "Super-parameterization": a better way to simulate regional extreme precipitation? J. Adv. Model Earth Syst. 4, 1–10.
Li, Q., Wang, T., Wang, F., et al., 2020. Dynamical downscaling simulation of the East Asian summer monsoon in a regional Climate-Weather Research and forecasting model. Int. J. Climatol. 1–17.
Li, Z., Tam, C.-Y., Li, Y., Lau, N.C., Chen, J., Chan, S.T., Lau, D.D.S., Huang, Y.Y., 2022. How does air-sea wave interaction affect tropical cyclone intensity? An atmosphere-wave-ocean coupled model study based on super typhoon Mangkhut (2018). Earth and Space Science 9, e2021EA002136.
Liang, X.Z., Xu, M., Yuan, X., Ling, T., Choi, H.I., Zhang, F., Chen, L., Liu, S.Y., Su, S.J., Qiao, F.X., He, Y.X., Wang, J.X.L., Kunkel, K.E., Gao, W., Joseph, E., Morris, V., Yu, T.W., Dudhia, J., Michalakes, J., 2012. Regional climate-weather research and forecasting model. Bull. Am. Meteorol. Soc. 93, 1363–1387.
Liang, X.Z., Sun, C., Zheng, X., Dai, Y., Xu, M., Choi, H.I., Ling, T., Qiao, F., Kong, X., Bi, X., Song, L., Wang, F., 2019. CWRF performance at downscaling China climate characteristics. Clim. Dyn. 52, 2159–2184.
Lumley, T., Miller, A., 2017. Leaps: regression subset selection. R package version 3.0. URL. https://CRAN.R-project.org/package=leaps.
Molod, A., Takacs, L., Suarez, M., Bacmeister, J., 2015. Development of the GEOS-5 atmospheric general circulation model: Evolution from MERRA to MERRA2. Geosci. Model Dev. 8, 1339–1356.
NASA/LARC/SD/ASDC, 2021. GEWEX SRB Integrated Product (Rel-4) Longwave Daily Average by UTC. https://doi.org/10.5067/GEWEXSRB/Rel4-IP_Longwave_daily_utc_1.
Nordeng, T.E., 1995. Extended version of the convective parameterization scheme at ECMWF and their impact on the mean and transient activity of the model in the Tropics. In: ECMWF Research Department Tech. Memo. 2006, p. 41.
Prein, A.F., Rasmussen, R.M., Ikeda, K., Liu, C., Clark, M.P., Holland, G.J., 2017. The future intensification of hourly precipitation extremes. Nat. Clim. Chan. 7, 48–52.
Qiao, F., Liang, X.Z., 2015. Efects of cumulus parameterizations on predictions of summer food in the Central United States. Clim. Dyn. 45, 727–744.
Qiao, F., Liang, X.Z., 2016. Effects of cumulus parameterization closures on simulations of summer precipitation over the United States coastal oceans. J. Adv. Model Earth Syst. 8, 764–785.
Qiao, F., Liang, X.Z., 2017. Effects of cumulus parameterization closures on simulations of summer precipitation over the continental United States. Clim. Dyn. 49, 225–247.
Reichle, R.H., Liu, Q., Koster, R.D., Draper, C.S., Mahanama, S.P., Partyka, G.S., 2017. Land surface precipitation in MERRA-2. J. Clim. 30, 1643–1664.
Rienecker, M.M., Suarez, M.J., Gelaro, R., Todling, R., Bacmeister, J., Liu, E., 2011. MERRA: NASA's modern-era retrospective analysis for research and applications. J. Clim. 24, 3624–3648.
Shen, X.Y., Huang, W., Qing, T., Huang, W.Y., Li, X.F., 2014. A modified scheme that parameterizes depositional growth of ice crystal: a modeling study of pre-summer torrential rainfall case over Southern China. Atmos. Res. 138, 293–300.
Shen, X.Y., Huang, W.Y., Guo, Y., Jiang, X.C., 2016. Precipitation responses to radiative effects of ice clouds: a cloud-resolving modeling study of a pre-summer torrential precipitation event. Adv. Atmos. Sci. 33 (10), 1137–1142.
Skamarock, W.C., Klemp, J.B., Dudhia, J., Gill, D.O., Barker, D., Duda, M.G., Huang, X.Y., Wang, W., Powers, J.G., 2008. A Description of the Advanced Research WRF Version 3. (No. NCAR/TN-475+STR).
Sun, C., Liang, X.Z., 2020a. Improving US extreme precipitation simulation: sensitivity to physics parameterizations. Clim. Dyn. 54, 4891–4918.
Sun, C., Liang, X.Z., 2020b. Improving US extreme precipitation simulation: dependence on cumulus parameterization and underlying mechanism. Clim. Dyn. 55, 1325–1352.
Sun, Y., Solomon, S., Dai, A., Portmann, R.W., 2006. How often does it rain? J. Clim. 19, 916–934.
Taylor, K.E., 2001. Summarizing multiple aspects of model performance in a single diagram. J. Geophys. Res. Atmos. 106, 7183–7192.
Tiedtke, M., 1989. A comprehensive mass flux scheme for cumulus parameterization in large-scale models. Mon. Weather Rev. 117, 1779–1800.
Tripathi, O.P., Dominguez, F., 2013. Effects of spatial resolution in the simulation of daily and subdaily precipitation in the southwestern US. J. Geophys. Res. Atmos. 118, 7591–7605.
Wang, Y., Li, H.X., Wang, H.J., Sun, B., Chen, H.P., 2021. Evaluation of CMIP6 model simulations of extreme precipitation in China and comparison with CMIP5. Acta Meteorol. Sin. 79, 369–386.
Wasserman, G.S., Sudjianto, A., 1994. All subsets regression using a genetic search algorithm. Comput. Ind. Eng. 27, 489–492.
Wilcox, E.M., Donner, L.J., 2007. The frequency of extreme rain events in satellite rain-rate estimates and an atmospheric general circulation model. J. Clim. 20, 53–69.
Wu, J., Gao, X.J., 2013. A gridded daily observation dataset over China region and comparison with the other datasets. Chin. J. Geophys. 56, 1102–1111.
Wu, J., Zhou, B.T., Xu, Y., 2015. Response of precipitation and its extremes over China to warming: CMIP5 simulation and projection. Chin. J. Geophys. 58, 3048–3060.
Xie, M.H., Zhang, J.S., Boyle, R.T., Cederwall, G.L., Potter, Lin, W.Y., 2004. Impact of a revised convective triggering mechanism on Community Atmosphere Model, Version 2, simulations: results from short-range weather forecasts. J. Geophys. Res. 109, D14102.
Xie, S.P., Deser, C., Vecchi, G.A., Collins, M., Delworth, T.L., Hall, A., Hawkins, E., Johnson, N.C., Cassou, C., Giannini, A., Watanabe, M., 2015. Towards predictive understanding of regional climate change. Nat. Clim. Chang. 5, 921–930.
Xu, C.H., Luo, Y., Xu, Y., 2011. Projected changes of precipitation extremes in river basins over China. Quat. Int. 244, 149–158.
Yao, W.R., Che, H.Z., Gui, K., Wang, Y.Q., Zhang, X.Y., 2020. Can MERRA-2 reanalysis data reproduce the three-dimensional evolution characteristics of a typical dust process in East Asia? A case study of the dust event in May 2017. Remote Sens. 12, 902.
Zeng, M.J., Lu, W.S., Liang, X.Z., Wang, X.L., 2008. Ensemble forecast experiment on precipitation in summer by CWRF numeric Model. Plateau Meteorology (in Chinese). 27, 1218–1228.

Zhang, H., 2019. Characteristics and Mechanisms of the Large-Scale and Convective Precipitation in Southern China. Lanzhou University.
Zhang, W.X., Zhou, T.J., 2020. Increasing impacts from extreme precipitation on population over China with global warming. Sci. Bull. 65, 243–252.
Zhao, C.Y., Xu, G.Q., 2020. The impact of scale-aware cumulus parameterization scheme on the numerical simulation of a squall line in the South China. Chinese J. Atmos. Sci (in Chinese). 44, 297–314.